Supplementary Information for Harnessing Forward Multiple Scattering for Optical Imaging Deep Inside an Opaque Medium

Ulysse Najar, Victor Barolle, Paul Balondrade,
Mathias Fink, Claude Boccara, and Alexandre Aubry
Institut Langevin, ESPCI Paris, PSL University, CNRS, Paris, France

Abstract

This document provides further information on: (*i*) the experimental set up; (*ii*) the theoretical analysis of the de-scanned and distortion matrices; (*iii*) the estimation of the transmittance matrix; (*iv*) the analysis of the transmittance matrix estimator; (*v*) the comparison with state-of-the-art methods; (*vi*) the notations of the paper.

1. DETAILED EXPERIMENTAL SET-UP

The full experimental set up is displayed in Supplementary Fig. 1. The setup is divided into two building blocks, labelled (a) and (b). The first component is a Michelson interferometer [Supplementary Fig. 1a]. The light source is a broadband LED (Thorlabs M850LP1, $\lambda_\circ = 850$ nm, $\Delta\lambda = 35$ nm), is placed in a plan conjugated with the focal plane within the sample, so as to illuminate the focal plane with the image of the source. The source's illumination pattern is not uniform and is smaller than the maximal extension of the field of view allowed by the microscope objectives' numerical aperture. As a result, the sample's intensity in the focal plane is modulated by the image of the source. In order to get a uniform illumination of the whole field of view, we set up a pseudo-Koehler illumination apparatus: An aspheric lens and a diaphragm are placed right in front of the source, such that the incident beam is collimated in the diaphragm plane. This plane is considered the source plane, and is conjugated to the sample plane by (L1). This way, the image of the source is defocused in the sample plane. This ensures an incoherent [1], yet uniform, illumination of the field of view.

The incident light is collimated using a converging lens (L1) with a focal length $f_1 = 150$ mm. The beam transmitted through this lens (L1) is linearly polarized at 45° by a polarizer (P1) so that it is then equally reflected (sample arm) and transmitted (reference arm) by the polarized beam splitter (PBS1).

The sample beam reflected by (PBS1) is horizontally polarized. It propagates through a quarter-wave plate (QWP1), is reflected by a plane mirror (M1), whose normal axis lies along the optical axis and that is mounted on a piezoelectric actuator (PZT). The reflected beam passes again through the quarter-wave plate (QWP1). This sequence induces a polarization rotation by 90° of the reflected beam with respect to the incident beam in the sample arm. The reflected wave can be then transmitted through the beam splitter (PBS1) with a vertical polarization and finally focused in a secondary source plane conjugated with the source plane by means of the lens (L2) of focal length $f_2 = 125$ mm.

The reference beam, vertically polarized at the exit of the polarizer (P1), is transmitted by the beam splitter (PBS1), propagates through a quarter-wave plate (QWP2), is reflected by a set of two galvanometric scan mirrors, and then by the reference mirror (M2). The set of scan mirrors enables a 2D rotation of the incident wave-field by angles $\mathbf{\Theta} = (\Theta_x, \Theta_y)$ with

respect to the optical axis. After reflection on the reference mirror (M2) and on the scan mirrors back again, the reflected beam propagates again through (QWP2). This round trip through (QWP2) enables a 90° rotation of the polarization: Whereas the incident light is V-polarized when it enters the reference arm, it is H-polarized when exiting it (see Fig. 1a). Therefore, the reference beam is reflected by the beam splitter (PBS1) before being focused by the lens (L2) in the secondary source plane.

Finally, in the secondary source plane, the wave-field is made of two images of the incident light orthogonally polarized and translated with respect to each other by a relative position $\Delta\boldsymbol{\rho} = (\Delta x, \Delta y)$. This lateral shift is dictated by the tilt $\boldsymbol{\Theta} = (\Theta_x, \Theta_y)$ of the reference beam: $\Delta x = 2f_2 \tan\Theta_x$ and $\Delta y = 2f_2 \tan\Theta_y$. The factor 2 results from the double reflection on each scan mirror, due to the reflection on the (M2) mirror. Note also that the optical path difference between the two arms is set to zero by equalizing the length of sample and reference arms for $\Delta\boldsymbol{\theta} = 0$.

After the Michelson interferometer, the two orthogonally polarized twin beams enter a Michelson interferometer with two identical microscope objectives in both arms (a configuration known as a Linnik interferometer) [Supplementary Fig. 1b]. They are again collimated by a lens (L3) of focal length f_3=200 mm. The two lenses (L2) and (L3) thus constitute a $4f$ system which compensates the effects of diffraction between the two interferometers.

The vertically polarized light (sample beam) is transmitted by a polarized beam splitter cube (PBS2), propagates through a quarter-wave plate (QWP4) before being focused in the focal plane of an immersion microscope objective (MO2, Nikon, 60×, NA=1.0). The light reflected by the sample is then collected by (MO2) and propagates again through the quarter-wave plate (QWP4). Because single scattering tends to preserve polarization, the corresponding wave-field undergoes a 90° polarization rotation and gets reflected by the beam splitter (PBS2) before being focused in the plane of the camera using the converging lens (L4) of focal length f_4 =200 mm. The combination of this lens (L4) with the microscope objective (MO1) entails a magnification M_4 of 60.

Regarding the horizontally-polarized beam at the exit of the lens (L3), it is reflected by the beam splitter (PBS2), passes through the quarter-wave plate (QWP3) before being focused by the microscope objective (MO1) identical to (MO2). The light is then reflected by the reference mirror (M3) placed in the focal plane of (MO2) before being collected again by the same microscope objective (MO2). The reflected light comes through the quarter-wave

plate (QWP3). As in the other arm, the polarization of the reflected beam exhibits a 90° rotation of its polarization. The beam is now vertically polarized and transmitted by the beam splitter (PBS2), before being focused on the camera with the lens (L4).

The detection scheme consists in recording the interferogram between the sample and reference beams based on their orthogonal polarisations projected through a 45-degree polarizer (P2). This experimental configuration allows an enhancement of single scattering and forward multiple scattering with respect to diffuse light in the sample arm. Indeed, the former components roughly exhibit the same time-of-flight and polarization as reference light while the latter one is characterized by a fully randomized polarization and a longer time-of-flight distribution. This filtering of diffuse light is deliberate since the post-processing method described in the accompanying paper addresses the forward multiple scattering contribution and not the randomly-scattered diffuse light.

The CMOS camera (Adimec Quartz 2A-750, 2Mpx) records the interferogram between sample and reference beams with a spatial sampling equal to δ_0 =230 nm given the magnification M_4. The volume of the sample from which photons can interfere with the reference beam is called the “coherence volume". Its position is dictated by the optical path difference between the reference and sample arms. Its thickness is inversely proportional to the light spectrum bandwidth [2]:

$$\delta z_t = \frac{2\ln 2}{n\pi}\left(\frac{\lambda_0^2}{\Delta\lambda}\right) \tag{1}$$

with λ_0 the central wavelength of the light source and $\Delta\lambda$ its spectral bandwidth. In the present case, $\delta z_t \sim 10$ μm. A critical tuning of the experimental set up consists in adjusting the coherence volume with the focal plane of the microscope objective. In a volumetric sample, whose refractive index differs from that of water, the coherence volume no longer coincides with the focusing plane. This focusing defect accumulates with the transverse aberrations generated by the heterogeneities of the medium. However, it is possible to compensate for it by a fine tuning of the length of the reference arm.

The experimental procedure then consists in recording the de-scanned reflection matrix $\mathbf{R}_{\text{in}}(z)$ at each depth z of the sample. This latter parameter is swept by means of a motorized axial displacement of the sample carrier. The scan of the relative position $\Delta\boldsymbol{\rho}$ between the incident wave-fields in the sample and reference arms is controlled by the tilt imposed by the galvanometer (M2). For each couple $(\Delta\boldsymbol{\rho}, z)$, the CCD camera conjugated with the MO

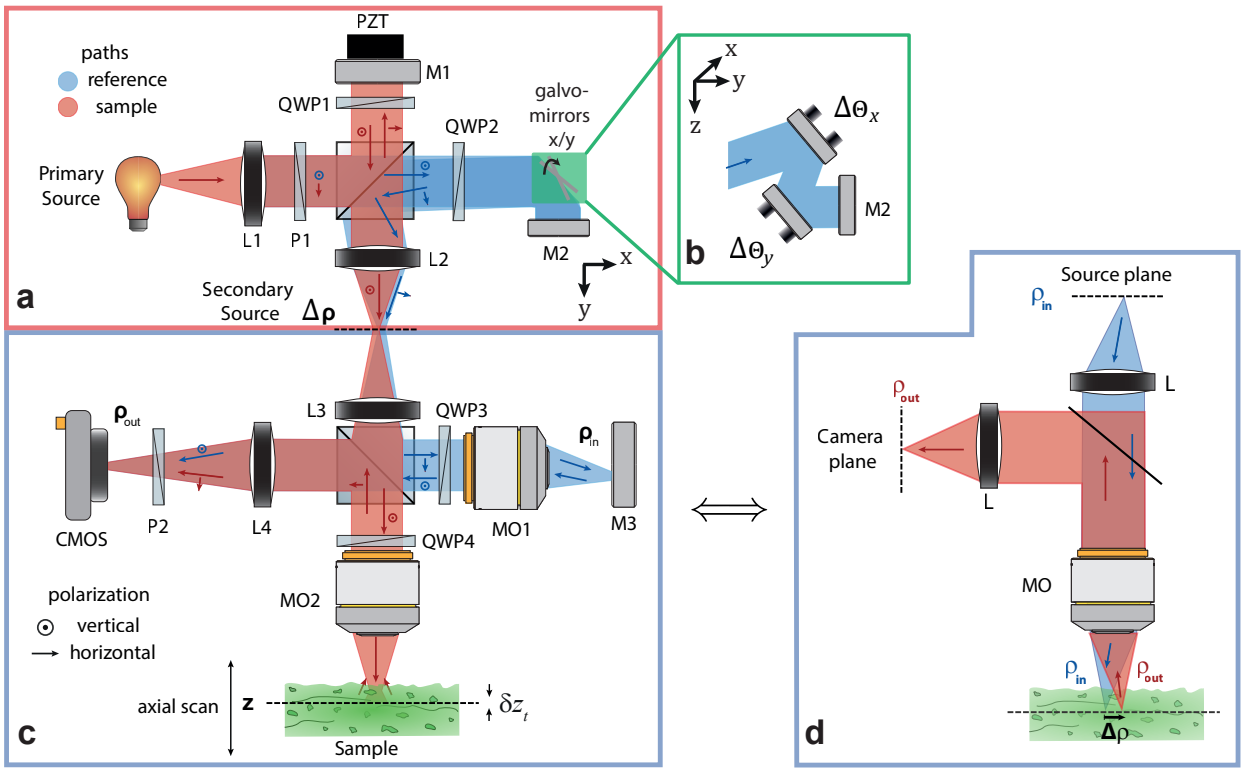
focal plane records the output intensity:

$$I_\alpha(\Delta\boldsymbol{\rho}, \boldsymbol{\rho}_{\rm out}, z) = \int_0^T |e^{i\alpha} E_{\rm out}(\boldsymbol{\rho}_{\rm out}, t) + E_{\rm out}^{(\rm ref)*}(\Delta\boldsymbol{\rho}, \boldsymbol{\rho}_{\rm out}, t)|^2 {\rm d}t \tag{2}$$

with t the absolute time, $\mathbf{r}$ the position vector on the CCD screen, $E_{\rm out}(\mathbf{r}, \tau)$ the scattered wave field associated with the sample arm, $E_{\rm out}^{(\rm ref)}(\mathbf{r}, \tau)$ the reference wave field; T the integration time of the CCD camera, and α an additional phase term controlled with a piezoelectric actuator placed on mirror (M1) of the first interferometer [Supplementary Fig. 1a]. The interference term between the sample and reference beams is extracted from the four intensity patterns (Eq. 2) recorded at $\alpha = 0$, $\pi/2$, $3\pi/2$ and π (phase-stepping interferometry) and provides the de-scanned wave-field:

$$R_{\rm in}(\Delta\boldsymbol{\rho}, \boldsymbol{\rho}_{\rm out}, z) = \frac{1}{T} \int_0^T E_{\rm out}(\boldsymbol{\rho}_{\rm out}, t) E_{\rm out}^{(\rm ref)*}(\Delta\boldsymbol{\rho}, \boldsymbol{\rho}_{\rm out}, t) {\rm d}t \tag{3}$$

Note that previous studies [3, 4] reported on the passive measurement of the de-scanned reflection matrix at the surface of a scattering sample. Although the experimental set up presented in those studies shares some similarities with the current set up displayed in Supplementary Fig. 1 (low-coherence interferometry), there are also several major differences. First, the two arms are illuminated by the light reflected by the sample in Ref. 3; hence there is no reference arm. Second, the reflection matrix is measured at the surface of the sample as a function of time-of-flight, while the current set up measures a time-gated reflection matrix as a function of depth inside the sample. At last, a much larger integration time is required to record the reflection matrix in Ref. [3] because of the absence of reference arm.



SUPPLEMENTARY FIGURE 1. **De-scanned measurement of the reflection matrix. a.** Experimental set up. P: polarizer, L: lens, QWP: quarter-wave plate, M: mirror, PZT: piezo-electric actuator, PBS: polarisation beam splitter, MO: microscope objective. The apparatus is made up of two parts (**a**,**b**). **a**. Michelson interferometer illuminated by an incoherent light source at its input and generating two twin incoherent beams of orthogonal polarization and laterally shifted from each other at its output. The polarised beam splitter (PBS1) separates the impinging light into a reference path (in blue) and a sample path (in red). The scan mirrors (inset in the green rectangle) tilt the reference beam by angles $\Delta\Theta_x$ and $\Delta\Theta_y$ in both transverse directions x and y. This allows the scan of the point-spread function along the de-scanned coordinates Δ_x and Δ_y in a plane conjugate to the reference mirror plane. **b**. Michelson interferometer with microscope objectives (MO) in both arms (Linnik configuration). Both beams have orthogonal polarizations and each interferometer arm includes a quarter-wave plate (QWP). The output beams are collected by the L4 lens and interfere on the camera after having been projected on a 45°-rotated polarizer (P2). **c**. Equivalent layout in the case of a coherent measurement. The source plane, the focal plane, and the camera planes are conjugated. Displacing a point source $\boldsymbol{\rho}_{\text{in}}$ in the source plane discretely scans the focal plane inside the sample. The illuminated area is imaged in the camera plane; in an epi-detection configuration.

2. THEORETICAL ANALYSIS

A. Theoretical expression of the de-scanned matrix

In this section, we express theoretically the de-scanned matrix recorded by the experimental set up in Supplementary Figs. 1a,b. To that aim, we will rely on the simple Fourier optics model proposed in a recent paper [5] to describe the manifestation of aberrations in FFOCT. For the sake of simplicity, this model is scalar. The large numerical aperture imposes that the recorded wave-field is associated with single scattering events taking place in the focal plane of the MO.

The wave field $E_{\text{out}}(\boldsymbol{\rho}_{\text{out}}, z)$ reflected by the sample arm in the camera plane can then be expressed as follows [5]:

$$E_{\text{out}}(\boldsymbol{\rho}_{\text{out}}, z, \omega) = \int_{\Sigma_0} \iint_{\Sigma_\rho} H(\boldsymbol{\rho}_{\text{out}}, \boldsymbol{\rho}_s, z)\gamma(\boldsymbol{\rho}_s, z)H(\boldsymbol{\rho}_s, \boldsymbol{\rho}_0, z)E_0(\boldsymbol{\rho}_0, \omega)\mathrm{d}\boldsymbol{\rho}_s\mathrm{d}\boldsymbol{\rho}_0. \tag{4}$$

$E_0(\boldsymbol{\rho}_0, \omega)$ is the incident wave-field in the secondary source plane Σ_0 at frequency ω. Light propagation between Σ_0 and the focal plane Σ_ρ is described by the impulse response $H(\boldsymbol{\rho}_0, \boldsymbol{\rho}_s, z)$ between a point in the secondary source plane at transverse coordinate $\boldsymbol{\rho}_0$ and a point at transverse coordinate $\boldsymbol{\rho}_s$ in the focal plane and at depth z inside the sample. It accounts for sample-induced aberrations. $\gamma(\boldsymbol{\rho}_s, z)$ represents the sample reflectivity at depth z. By spatial reciprocity, the propagation of the reflected wave-field from the sample to the detector plane is also modelled by the impulse response $H(\boldsymbol{\rho}_s, \boldsymbol{\rho}_{\text{out}})$. The relatively narrow bandwidth ($\Delta\lambda \ll \lambda$) of the light source and the use of achromatic optical elements (lens, beam splitter, quarter wave plate) allow us to neglect the dependence of H on frequency ω.

Replacing $\gamma(\boldsymbol{\rho}_s, z)$ by a uniform reflectivity in Eq. 4 and taking into account the lateral shift of the reference wave-field induced by the galvanometer M2 [Supplementary Fig. 1] leads to the following previous expression for $E_{\text{out}}^{(\text{ref})}(\boldsymbol{\rho}_{\text{out}}, z)$ [5]:

$$E_{\text{out}}^{(\text{ref})}(\boldsymbol{\rho}_{\text{out}}, \Delta\boldsymbol{\rho}, z) = \iint_{\Sigma_0} H_{\text{ref}}(\boldsymbol{\rho}_{\text{out}} - \boldsymbol{\rho}_0)E_0(\boldsymbol{\rho}_0 + \Delta\boldsymbol{\rho})\mathrm{d}\boldsymbol{\rho}_0. \tag{5}$$

where H_{ref} is the impulse response associated with the reference arm (way and return path) that we assume as spatially-invariant [$H_{\text{ref}}(\boldsymbol{\rho}_{\text{out}}, \boldsymbol{\rho}_0) = H_{\text{ref}}(\boldsymbol{\rho}_{\text{out}} - \boldsymbol{\rho}_0)$].

The de-scanned wave-field is obtained by extracting the interference term between the reflected wave-fields coming from the sample and reference arms:

$$R_{\text{in}}(\boldsymbol{\rho}_{\text{out}}, \Delta\boldsymbol{\rho}, z) = \langle E_{\text{out}}(\boldsymbol{\rho}_{\text{out}}, \omega)E_{\text{out}}^{(\text{ref})*}(\boldsymbol{\rho}_{\text{out}}, \omega)\rangle \tag{6}$$

Assuming a spatially-incoherent incident wave-field [$\langle E_0(\boldsymbol{\rho}_0)E_0^*(\boldsymbol{\rho}_0')\rangle = I_0\delta(\boldsymbol{\rho}_0 - \boldsymbol{\rho}_0')$] and injecting Eqs. 4 and 5 into the last equation leads to the following expression for the coefficients of $\mathbf{R}_{\text{in}}$:

$$R_{\text{in}}(\boldsymbol{\rho}_{\text{out}}, \Delta\boldsymbol{\rho}, z) = I_0 \iint H_{\text{out}}(\boldsymbol{\rho}_{\text{out}}, \boldsymbol{\rho}, z)\gamma(\boldsymbol{\rho}_s, z)H_{\text{in}}(\boldsymbol{\rho}_s, \boldsymbol{\rho}_{\text{out}} + \Delta\boldsymbol{\rho}, z)\mathrm{d}\boldsymbol{\rho} \tag{7}$$

with

$$H_{\text{out}} \equiv H \text{ and } H_{\text{in}} \equiv H \odot H_{\text{ref}}^*. \tag{8}$$

The symbol $\odot$ stands for the convolution product over the variable $\boldsymbol{\rho}_{\text{in}}$. The last equation means that: (i) the output focusing matrix, $\mathbf{H}_{\text{out}}$, and the associated $\mathbf{T}-$matrix, $\mathbf{T}_{\text{out}} = \mathbf{T}_0 \times \mathbf{H}_{\text{out}}$, only grasp the sample-induced aberrations; (ii) the input focusing matrix, $\mathbf{H}_{\text{in}}$, and the associated $\mathbf{T}-$matrix, $\mathbf{T}_{\text{in}} = \mathbf{T}_0 \times \mathbf{H}_{\text{in}}$, also contain the aberrations undergone by the incident and reflected reference beams (Supplementary Section 4 A).

For $\Delta\boldsymbol{\rho} = \mathbf{0}$ (conventional FFOCT set up), the recorded wave-field (Eq. 7) is equivalent to a time-gated confocal image [5]. It can actually be expressed as the convolution between the sample reflectivity γ and the confocal PSF $H_{\text{in}} \times H_{\text{out}}$:

$$R_{\text{in}}(\boldsymbol{\rho}_{\text{out}}, \Delta\boldsymbol{\rho} = \mathbf{0}, z) = I_0 \iint H_{\text{out}}(\boldsymbol{\rho}_{\text{out}}, \boldsymbol{\rho}_s, z)H_{\text{in}}(\boldsymbol{\rho}_s, \boldsymbol{\rho}_{out}, z)\gamma(\boldsymbol{\rho}_s, z)\mathrm{d}\boldsymbol{\rho}_s. \tag{9}$$

On the one hand, the confocal nature of the recorded wave-field implies a transverse resolution $\delta\rho_0 \sim \lambda/4\text{NA}$. On the other hand, the axial resolution is either controlled by the thickness δz_t of the coherence volume or the depth-of-field δz_0 of the microscope objective: $\delta z_0 = n\lambda/\text{NA}^2$. In the present case, $\delta z_0 \sim 1$ μm$< \delta z_t \sim 10$ μm. The axial resolution is thus given by the depth-of-field. $\delta\rho_0$ and δz_0 thus dictate the values of the transverse and axial sampling of the de-scanned matrix $\mathbf{R}_{\text{in}}$ in our experiment.

B. Relation between the de-scanned matrix and the focused reflection matrix

In this section, we investigate to which extent the de-scanned matrix recorded by the experimental set up in Supplementary Figs. 1a,b can be considered equivalent to the focused reflection matrix that would be recorded by the fictitious coherent set up displayed in Supplementary Fig. 1c.

The coefficients of a focused reflection matrix recorded by the fictitious coherent set up displayed in Fig. 1 can be expressed as:

$$R(\boldsymbol{\rho}_{\text{out}}, \boldsymbol{\rho}_{\text{in}}, z) = I_0 \iiint H(\boldsymbol{\rho}_{out}, \boldsymbol{\rho}_s, z)\gamma(\boldsymbol{\rho}_s, z)H(\boldsymbol{\rho}_s, \boldsymbol{\rho}_{in}, z)\mathrm{d}\boldsymbol{\rho} \tag{10}$$

A strict equality between Eqs. 7 and 10 is only obtained if $H_{\text{in}} \equiv H$. This condition is fulfilled only for a perfect reference arm: $\mathcal{T}_{\text{ref}} \equiv \mathbf{1}_{k<NA}$ and $H \odot H^*_{\text{ref}} \equiv H$. In theory, the incoherent set up of Fig. 1a is thus equivalent to the fictitious coherent set up of Fig. 1b.

$$R_{\text{in}}(\Delta\boldsymbol{\rho}, \boldsymbol{\rho}_{\text{out}}) = R(\boldsymbol{\rho}_{\text{out}} + \Delta\boldsymbol{\rho}, \boldsymbol{\rho}_{\text{out}}, z) \tag{11}$$

In reality, the reference arm always exhibits aberrations such as a slight defocus of the reference mirror M3 in Fig. 1b or a slight defocus of the reference beam in the secondary source plane at the output of first interferometer.

C. The distortion matrix

The distortion matrix is related to the de-scanned matrix by a simple Fourier transform:

$$\mathbf{D}_{\text{in}}(z) = \mathbf{T}_0 \times \mathbf{R}_{\text{in}}(z), \tag{12}$$

or in terms of matrix coefficients,

$$D(\mathbf{u}_{\text{in}}, \boldsymbol{\rho}_{\text{out}}, z) = \sum_{\Delta\boldsymbol{\rho}} R_{\text{in}}(\Delta\boldsymbol{\rho}, \boldsymbol{\rho}_{\text{out}}, z) \exp\left(-i\frac{2\pi}{\lambda f}\mathbf{u}_{\text{in}} \cdot \Delta\boldsymbol{\rho}\right). \tag{13}$$

Injecting Eq. 7 into the last equation yields

$$D(\mathbf{u}_{\text{in}}, \boldsymbol{\rho}_{\text{out}}, z) = \sum_{\Delta\boldsymbol{\rho}} I_0 \iint H_{\text{out}}(\boldsymbol{\rho}_{\text{out}}, \boldsymbol{\rho}_s, z)\gamma(\boldsymbol{\rho}_s, z)H_{\text{in}}(\boldsymbol{\rho}_s, \boldsymbol{\rho}_{out}+\Delta\boldsymbol{\rho}, z) \exp\left(-i\frac{2\pi}{\lambda f}\mathbf{u}_{\text{in}} \cdot \Delta\boldsymbol{\rho}\right) \mathrm{d}\boldsymbol{\rho}_s. \tag{14}$$

In a previous paper [6], we showed that a singular value decomposition of $\mathbf{D}$ enables to decompose the field-of-view into isoplanatic modes and extract the associated aberration

phase laws. However, this demonstration was based on the condition that the $\mathbf{D}-$matrix is dominated by its correlations in the focal plane. This is the case for a specular reflector such as a resolution target or a medium of continuous reflectivity but no longer valid for a random distribution of heterogeneities like in the opaque cornea under study. In the accompanying paper, we propose a more general solution to overcome aberrations and scattering in optical microscopy: An iterative multi-scale analysis of wave distortions.

To that aim, the field-of-detection should be subdivided into overlapping regions that are defined by their central midpoint $\mathbf{r}_p = (\boldsymbol{\rho}_p, z_p)$ and their spatial extension L. All of the distorted components associated with focusing points $\boldsymbol{\rho}_{\text{out}}$ located within each region are extracted and stored in a local distortion matrix $\mathbf{D}'_{\text{in}}(\mathbf{r}_p)$:

$$D'(\mathbf{u}_{\text{in}}, \boldsymbol{\rho}_{\text{out}}, \mathbf{r}_p) = D(\mathbf{u}_{\text{in}}, \boldsymbol{\rho}_{\text{out}}, z_p)\ W_L(\boldsymbol{\rho}_{\text{out}} - \boldsymbol{\rho}_p), \tag{15}$$

where $W_L(x, y) = 1$ for $|x| < L$ and $|y| < L$, and zero otherwise.

At this stage, a local isoplanatic assumption shall be made over each region of size L. This hypothesis implies that the PSFs $H_{\text{in/out}}$ are invariant by translation in each region. This leads us to define local spatially-invariant PSFs $H^{(l)}_{\text{in/out}}$ around each central midpoint $\mathbf{r}_{\text{p}}$ such that:

$$H_{\text{in/out}}(\boldsymbol{\rho}_s, \boldsymbol{\rho}_{\text{in/out}}, z_p) = H^{(l)}_{\text{in/out}}(\boldsymbol{\rho}_s - \boldsymbol{\rho}_{\text{in/out}}, \mathbf{r}_p). \tag{16}$$

Under this assumption, Eq. 14 can be rewritten as follows:

$$D'(\mathbf{u}_{\text{in}}, \boldsymbol{\rho}_{\text{out}}, \mathbf{r}_{\text{p}}) = \underbrace{\mathcal{T}_{\text{in}}(\mathbf{u}_{\text{in}}, \mathbf{r}_{\text{p}})}_{\text{transmittance}} \underbrace{\iint \gamma(\boldsymbol{\rho}_s + \boldsymbol{\rho}_{\text{out}}, z) H^{(l)}_{\text{out}}(\boldsymbol{\rho}_s, \mathbf{r}_p) \exp\left(-i\frac{2\pi}{\lambda f}\mathbf{u}_{\text{in}} \cdot \boldsymbol{\rho}\right) \mathrm{d}\boldsymbol{\rho}_s}_{\text{virtual source}}. \tag{17}$$

Around each point $\mathbf{r}_{\text{p}}$, the aberrations can be modelled by a local transmittance $\mathcal{T}_{\text{in}}(\mathbf{u}_{\text{in}}, \mathbf{r}_{\text{p}})$. This transmittance is the Fourier transform of the input PSF $H^{(l)}_{\text{in}}(\boldsymbol{\rho}_s, \mathbf{r}_{\text{p}})$:

$$\mathcal{T}_{\text{in}}(\mathbf{u}_{\text{in}}, \mathbf{r}_{\text{p}}) = \iint H^{(l)}_{\text{in}}(\boldsymbol{\rho}_s, \mathbf{r}_{\text{p}}) \exp\left(\frac{2\pi}{\lambda f}\mathbf{u}_{\text{in}} \cdot \boldsymbol{\rho}_s\right) \mathrm{d}\boldsymbol{\rho}_s \tag{18}$$

The physical meaning of this last equation is the following: Each distorted wave-field corresponds to the diffraction of a virtual source synthesized inside the medium modulated by the pupil transmittance $\mathcal{T}_{\text{in}}(\mathbf{u}_{\text{in}}, \mathbf{r}_{\text{p}})$ of the sample seen from point $\mathbf{r}_{\text{p}}$. Each virtual source is spatially incoherent due to the random reflectivity of the medium, and its size is governed by the spatial extension of the output focal spot. The idea is now to smartly combine each

virtual source to generate a coherent guide star and estimate the local transmittance $\mathcal{T}_{\rm in}$ independently from the sample reflectivity.

D. Covariance Matrix of Wave Distortions

To do so, the correlation matrix $\mathbf{C}_{\rm in} = \mathbf{D}_{\rm in}\mathbf{D}_{\rm in}^{\dagger}$ is an excellent tool. Its coefficients write as follows

$$C_{\rm in}(\mathbf{u}_{\rm in}, \mathbf{u}'_{\rm in}, \mathbf{r}_{\rm p}) = N_{\mathcal{W}}^{-1} \sum_{\boldsymbol{\rho}_{\rm out}} D'(\mathbf{u}_{\rm in}, \boldsymbol{\rho}_{\rm out}, \mathbf{r}_{\rm p}) D'^{*}(\mathbf{u}'_{\rm in}, \boldsymbol{\rho}_{\rm out}, \mathbf{r}_{\rm p}) \tag{19}$$

The matrix $\mathbf{C}_{\rm in}(\mathbf{r}_{\rm p})$ can be decomposed as the sum of its ensemble average, the covariance matrix $\langle \mathbf{C}_{\rm in} \rangle (\mathbf{r}_p)$, and a perturbation term $\delta\mathbf{C}_{\rm in}(\mathbf{r}_p)$:

$$\mathbf{C}_{\rm in}(\mathbf{r}_p) = \langle \mathbf{C}_{\rm in} \rangle (\mathbf{r}_p) + \delta\mathbf{C}_{\rm in}(\mathbf{r}_p). \tag{20}$$

The intensity of the perturbation term scales as the inverse of the number $N_{\rm W} = (L/\delta\rho_0)^2$ of resolution cells in each sub-region [7, 8]:

$$\left\langle \left| \delta C_{\rm in}(\mathbf{u}, \mathbf{u}', \mathbf{r}_p) \right|^2 \right\rangle = \frac{\left\langle \left| C_{\rm in}(\mathbf{u}, \mathbf{u}, \mathbf{r}_p) \right|^2 \right\rangle}{N_{\mathcal{W}}} \tag{21}$$

This perturbation term can thus be reduced by increasing the size L of the spatial window W_L, but at the cost of a resolution loss.

Under assumptions of local isoplanicity (Eqs. 16 and 17) and random reflectivity,

$$\langle \gamma(\boldsymbol{\rho}_s, z) \gamma^*(\boldsymbol{\rho}'_s, z) \rangle = \langle |\gamma|^2 \rangle \delta(\boldsymbol{\rho}_s - \boldsymbol{\rho}'_s), \tag{22}$$

with δ, the Dirac distribution, the covariance matrix can be expressed as follows [9]:

$$\langle \mathbf{C}_{\rm in} \rangle (\mathbf{r}_{\rm p}) = \left[\boldsymbol{\mathcal{T}}_{\rm in}(\mathbf{r}_{\rm p}) \circ \mathbf{T}_0 \right] \times \mathbf{C}_H(\mathbf{r}_{\rm p}) \times \left[\mathbf{T}_0 \circ \boldsymbol{\mathcal{T}}_{\rm in}(\mathbf{r}_{\rm p}) \right]^{\dagger}, \tag{23}$$

or, in terms of matrix coefficients,

$$\begin{aligned} \langle \mathbf{C}_{\rm in} \rangle (\mathbf{u}_{\rm in}, \mathbf{u}'_{\rm in}, \mathbf{r}_{\rm p}) &= \mathcal{T}_{\rm in}(\mathbf{u}_{\rm in}, \mathbf{r}_{\rm p}) \mathcal{T}^*_{\rm in}(\mathbf{u}'_{\rm in}, \mathbf{r}_{\rm p}) \iint \mathrm{d}\boldsymbol{\rho}_s \left| H^{(l)}_{\rm out}(\boldsymbol{\rho}_s, \mathbf{r}_{\rm p}) \right|^2 \exp\left[-i \frac{2\pi}{\lambda f} (\mathbf{u}_{\rm in} - \mathbf{u}'_{\rm in}) \cdot \boldsymbol{\rho}_s \right] \\ &= \mathcal{T}_{\rm in}(\mathbf{u}_{\rm in}, \mathbf{r}_{\rm p}) \mathcal{T}^*_{\rm in}(\mathbf{u}'_{\rm in}, \mathbf{r}_{\rm p}) \underbrace{\left[\mathcal{T}_{\rm out} \overset{\mathbf{u}}{\circledast} \mathcal{T}_{\rm out} \right] (\mathbf{u}_{\rm in} - \mathbf{u}'_{\rm in}, \mathbf{r}_{\rm p})}_{= C_H(\mathbf{u}_{\rm in}, \mathbf{u}'_{\rm in}, \mathbf{r}_{\rm p})}. \end{aligned} \tag{24}$$

$\mathbf{C}_H$ is a reference correlation matrix that would be measured in an homogeneous cornea for a virtual reflector whose scattering distribution corresponds to the output focal spot intensity $|H^{(l)}_{\rm out}(\boldsymbol{\rho}_s, \mathbf{r}_{\rm p})|^2$. The covariance matrix $\langle \mathbf{C}_{\rm in} \rangle (\mathbf{r}_{\rm p})$ thus corresponds to the same experimental situation but for a virtual reflector embedded into the heterogeneous cornea under study.

3. ESTIMATION OF THE TRANSMITTANCE MATRIX

A. Iterative Time Reversal

For such an experimental configuration, it has been shown that an iterative time reversal (ITR) process converges towards a wavefront that focuses perfectly through the heterogeneous medium onto this scatterer [10, 11]. Hence, let us consider the following fictitious experiment that consists in a phase conjugating mirror placed in the pupil plane of the microscope objective and the virtual reflector placed in its focal plane (see Supplementary Fig. 2b). It gives rise to a stationary wave-field, $\boldsymbol{\psi} = \boldsymbol{\psi}^+ + \boldsymbol{\psi}^-$, made of down-going and up-going wave-fields, $\boldsymbol{\psi}^-$ and $\boldsymbol{\psi}^+$. Both wave-fields check the following relationships in the pupil plane:

$$\boldsymbol{\psi}^+_{\mathrm{u}} = \mathbf{C}_{\mathrm{in}} \times \boldsymbol{\psi}^-_{\mathrm{u}} \tag{25}$$

and

$$\psi^-_{\mathbf{u}} = \epsilon \psi^{+*}_{\mathbf{u}}. \tag{26}$$

with ϵ the reflectivity of the phase conjugating mirror. Combining the two previous equations leads to the following eigenequation:

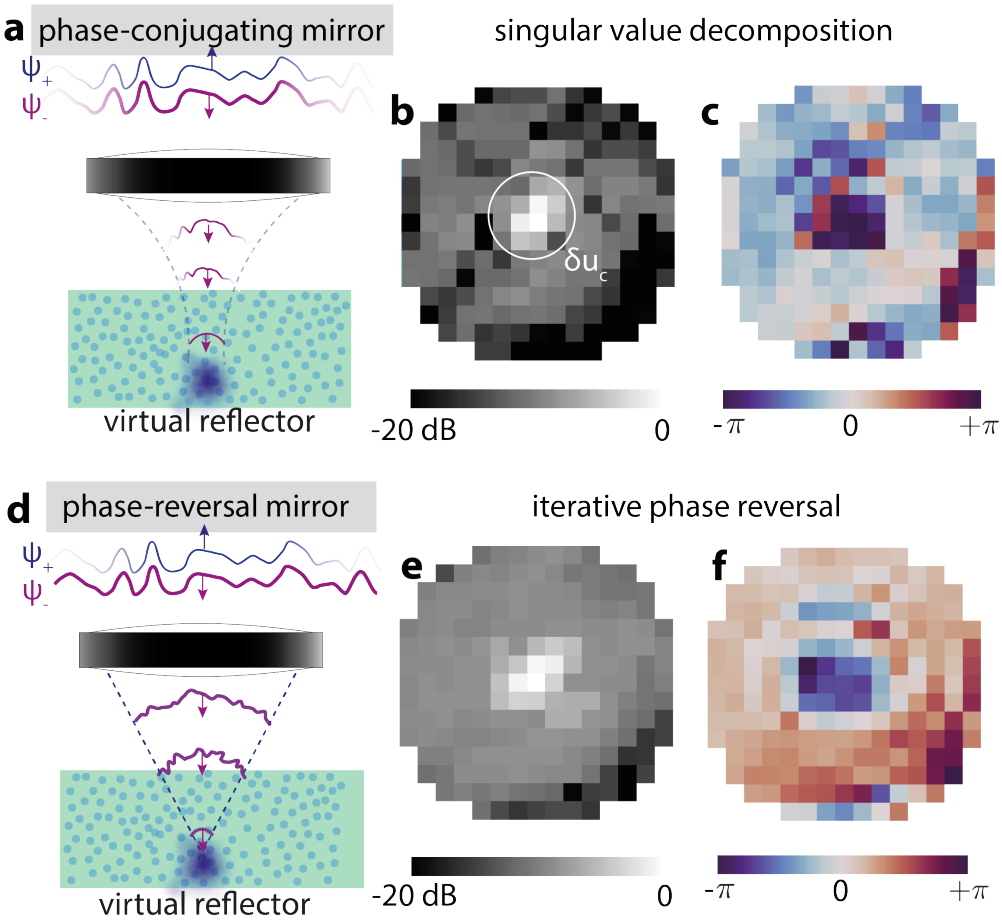
$$\boldsymbol{\psi}^-_{\mathbf{u}} = |\epsilon|^2 \mathbf{C}^*_{\mathrm{in}} \mathbf{C}_{\mathrm{in}} \times \boldsymbol{\psi}^-_{\mathbf{u}}. \tag{27}$$

The ITR process has thus eigenmodes which can be determined by the diagonalization of the time reversal operator $\mathbf{C}^*_{\mathrm{in}}\mathbf{C}_{\mathrm{in}}$. In particular, the first eigenvector $\mathbf{U}_{\mathrm{in}}$ of $\mathbf{C}^*_{\mathrm{in}}\mathbf{C}_{\mathrm{in}}$, which is also the first singular vector of $\mathbf{D}_{\mathrm{in}}$, corresponds to the wave-front that optimizes the energy backscattered by the virtual reflector.

If the virtual reflector was point-like, this wave-front would be a perfect estimator of $\mathcal{T}_{\mathrm{in}}$. Its phase conjugate would perfectly compensate for aberrations and focuses through the heterogeneous medium onto the point-like target [10, 11]. However, here the virtual guide star is enlarged compared to the diffraction limit. This wave-front is of finite angular support δu_c and tends to focus on the virtual reflector but with a resolution width $\delta\rho_c \sim \lambda f/\delta u_c$ larger than the diffraction limit [8] (see Supplementary Fig. 2). Its phase is thus a good estimator of $\mathcal{T}_{\mathrm{in}}$ over the angular domain δu_c but absolutely not elsewhere.

This assertion is illustrated by Supplementary Figs. 2b and c that show the modulus and phase of the first singular vector $\mathbf{U}_{\mathrm{in}}$ of $\mathbf{D}_{\mathrm{in}}$ at depth $z = 200$ μm in the cornea. As

anticipated, the modulus of $\mathbf{U}_{\text{in}}$ exhibits a main central lobe at small spatial frequencies (delimited by a circle white line in Supplementary Fig. 2b) but is extremely low at high angles of incidence. This means that the phase of $\mathbf{U}_{\text{in}}$ is a good estimator for $|\mathbf{u}_{\text{in}}| < \delta u_c$ but is not reliable beyond u_c (Supplementary Fig. 2c).



SUPPLEMENTARY FIGURE 2. **Iterative Time Reversal vs. Iterative Phase Reversal.** **a.** The first eigenstate of $\mathbf{C}_{\text{in}}$ corresponds to the eigenmode that would arise between a phase conjugating mirror in the pupil plane and the virtual reflector. **b-c.** Absolute value and phase of $\mathbf{U}_1$ the first eigenvector of $\mathbf{C}_{\text{in}}$ at the first iteration of the multi-scale analysis ($z = 200$ μm). **d.** The IPR process converges towards the wave-front $\hat{\mathcal{T}}_{\text{in}}$ that would be obtained if an iterative phase reversal mirror was used to focus on the virtual reflector. **e-f.** Absolute value of $\mathbf{C}_{\text{in}} \times \hat{\mathcal{T}}_{\text{in}}$ and phase of $\hat{\mathcal{T}}_{\text{in}}$ at the first iteration of the multi-scale analysis ($z = 200$ μm).

B. Iterative Phase Reversal

To circumvent that issue, the iterative phase reversal (IPR) algorithm has been developed. It consists in replacing the virtual phase conjugating mirror of Supplementary Fig. 2a by a phase reversal mirror (Supplementary Fig. 2b). As a phase conjugating mirror, the latter mirror reverses the phase of the incident wave-field but back-emits a wave of constant amplitude, such that:

$$\psi_{\mathbf{u}}^{-} = \exp\left[i \arg\left\{\psi_{\mathbf{u}}^{+*}\right\}\right]. \tag{28}$$

Combined with Eq. 25, the latter equation yields the following relation for the down-going wave-field:

$$\psi_{\mathbf{u}}^{-} = \exp\left[i \arg\left\{\mathbf{C}_{\text{in}} \times \boldsymbol{\psi}_{\text{u}}^{-}\right\}\right]. \tag{29}$$

Unlike Eq. 27, this is not an eigenequation but it can be solved iteratively [see Eq. 18 of the accompanying manuscript]. By definition, the resulting wave-front $\hat{\mathcal{T}}_{\text{in}}$ is of constant modulus over the pupil. To see the angular domain addressed by $\hat{\mathcal{T}}_{\text{in}}$, one can investigate the modulus of $\mathbf{C}_{\text{in}} \times \hat{\mathcal{T}}_{\text{in}}$ (see Supplementary Fig. 2e). Comparison with Supplementary Fig. 2b shows that the IPR process addresses each angular component of the imaging process, leading to a more reliable estimation of the $\mathbf{T}-$matrix over the whole pupil (Supplementary Fig. 2f). While ITR is guided by a maximization of the energy back-scattered by the virtual reflector, IPR optimizes the coherence of the wave-front over the whole pupil aperture, thereby leading, in principle, to a diffraction-limited focal spot onto the virtual scatterer (Supplementary Fig. 2c).

In Supplementary Section 5 B, the IPR and ITR approaches will be compared quantitatively when incorporated in a multi-scale process. Prior to that, the bias of the $\mathbf{T}-$matrix estimator provided by IPR is established theoretically to justify this strategy.

C. Bias of the $\mathcal{T}$-matrix estimator

The IPR process assumes the convergence of the correlation matrix $\mathbf{C}_{\text{in}}$ (Eq. 10) towards its ensemble average $\langle \mathbf{C}_{\text{in}} \rangle$, the covariance matrix [8, 9]. In fact, this convergence is never fully realized and $\mathbf{C}_{\text{in}}$ should be decomposed as the sum of this covariance matrix $\langle \mathbf{C}_{\text{in}} \rangle$ and the perturbation term $\delta\mathbf{C}_{\text{in}}$ (Eq. 20). In the following, we express theoretically the bias induced by this perturbation term on the estimation of $\hat{\boldsymbol{\mathcal{T}}}_{\text{in}}$. In particular, we will show

how it scales with the parameter $N_{\mathcal{W}}$ and the focusing quality. We consider here the input correlation matrix $\mathbf{C}_{\text{in}}$ but a similar demonstration can be performed at output. For sake of lighter notation, the dependence over $\mathbf{r}_p$ is omitted in the following.

To understand the parameters controlling the error $\delta\boldsymbol{\mathcal{T}}_{\text{in}}$ between $\hat{\boldsymbol{\mathcal{T}}}_{\text{in}}$ and $\boldsymbol{\mathcal{T}}_{\text{in}}$, one can express $\hat{\boldsymbol{\mathcal{T}}}_{\text{in}}$ as follows:

$$\hat{\boldsymbol{\mathcal{T}}}_{\text{in}} = \exp\left(j\arg\left\{\mathbf{C}_{\text{in}} \times \hat{\boldsymbol{\mathcal{T}}}_{\text{in}}\right\}\right) = \frac{\mathbf{C}_{\text{in}} \times \hat{\boldsymbol{\mathcal{T}}}_{\text{in}}}{||\mathbf{C}_{\text{in}} \times \hat{\boldsymbol{\mathcal{T}}}_{\text{in}}||} \tag{30}$$

By injecting Eq. 20 into the last expression, $\hat{\boldsymbol{\mathcal{T}}}_{\text{in}}$ can be expressed, at first order, as the sum of its expected value $\boldsymbol{\mathcal{T}}_{\text{in}}$ and a perturbation term $\delta\boldsymbol{\mathcal{T}}_{\text{in}}$:

$$\hat{\boldsymbol{\mathcal{T}}}_{\text{in}} = \underbrace{\frac{\langle\mathbf{C}_{\text{in}}\rangle \times \boldsymbol{\mathcal{T}}_{\text{in}}}{||\langle\mathbf{C}_{\text{in}}\rangle \times \boldsymbol{\mathcal{T}}_{\text{in}}||}}_{=\boldsymbol{\mathcal{T}}_{\text{in}}} + \underbrace{\frac{\delta\mathbf{C}_{\text{in}} \times \boldsymbol{\mathcal{T}}_{\text{in}}}{||\langle\mathbf{C}_{\text{in}}\rangle \times \boldsymbol{\mathcal{T}}_{\text{in}}||}}_{\simeq\delta\boldsymbol{\mathcal{T}}_{\text{in}}}. \tag{31}$$

The bias intensity can be expressed as follows:

$$|\delta\mathcal{T}_{\text{in}}|^2 = \frac{\boldsymbol{\mathcal{T}}_{\text{in}}^\dagger \times \delta\mathbf{C}_{\text{in}}^\dagger \times \delta\mathbf{C}_{\text{in}} \times \boldsymbol{\mathcal{T}}_{\text{in}}}{\boldsymbol{\mathcal{T}}_{\text{in}}^\dagger \times \langle\mathbf{C}_{\text{in}}\rangle^\dagger \times \langle\mathbf{C}_{\text{in}}\rangle \times \boldsymbol{\mathcal{T}}_{\text{in}}} \tag{32}$$

Using Eq. 21, the numerator of the previous equation can be expressed as follows:

$$\boldsymbol{\mathcal{T}}_{\text{in}}^\dagger \times \delta\mathbf{C}_{\text{in}}^\dagger \times \delta\mathbf{C}_{\text{in}} \times \boldsymbol{\mathcal{T}}_{\text{in}} = M^2\langle|\delta C_{\text{in}}(\mathbf{u},\mathbf{u}')|^2\rangle = M^2\langle|\langle C_{\text{in}}\rangle(\mathbf{u},\mathbf{u})|^2\rangle/N_{\mathcal{W}}. \tag{33}$$

Injecting Eq. 24 into the last equation leads to the following expression for the numerator of Eq. 32:

$$\boldsymbol{\mathcal{T}}_{\text{in}}^\dagger \times \delta\mathbf{C}_{\text{in}}^\dagger \times \delta\mathbf{C}_{\text{in}} \times \boldsymbol{\mathcal{T}}_{\text{in}} = M^2\left|\mathcal{T}_{\text{out}} \overset{\mathbf{u}}{\circledast} \mathcal{T}_{\text{out}}(\mathbf{0})\right|^2/N_{\mathcal{W}}. \tag{34}$$

The denominator of Eq. 32 can be expressed as follows:

$$\boldsymbol{\mathcal{T}}_{\text{in}}^\dagger \times \langle\mathbf{C}_{\text{in}}\rangle^\dagger \times \langle\mathbf{C}_{\text{in}}\rangle \times \boldsymbol{\mathcal{T}}_{\text{in}} = M^2\left|\sum_{\mathbf{u}} \mathcal{T}_{\text{out}} \overset{\mathbf{u}}{\circledast} \mathcal{T}_{\text{out}}(\mathbf{u})\right|^2 \tag{35}$$

The bias intensity is thus given by:

$$|\delta\mathcal{T}_{\text{in}}|^2 = \frac{\left|\mathcal{T}_{\text{out}} \overset{\mathbf{u}_{\text{out}}}{\circledast} \mathcal{T}_{\text{out}}(\mathbf{0})\right|^2}{N_{\mathcal{W}}\left|\sum_{\mathbf{u}} \mathcal{T}_{\text{out}} \overset{\mathbf{u}}{\circledast} \mathcal{T}_{\text{out}}(\mathbf{u})\right|^2} \tag{36}$$

In the last expression, we recognize the ratio between the coherent intensity (energy deposited exactly at focus) and the mean incoherent intensity. This quantity is known as the coherence factor in ultrasound imaging [7, 12]:

$$\mathcal{C}_{\text{out}} = \frac{\sum_{\mathbf{u}} \mathcal{T}_{\text{out}} \overset{\mathbf{u}}{\circledast} \mathcal{T}_{\text{out}}(\mathbf{u})}{\mathcal{T}_{\text{out}} \overset{\mathbf{u}}{\circledast} \mathcal{T}_{\text{out}}(\mathbf{0})} = \frac{|H_{\text{out}}^{(l)}(\boldsymbol{\rho}=\mathbf{0})|^2}{\delta_R^{-2}\int d\boldsymbol{\rho}|H_{\text{out}}^{(l)}(\boldsymbol{\rho})|^2} \tag{37}$$

In the speckle regime (Eq. 22) and for 3D imaging, the coherence factor $\mathcal{C}$ ranges from 0, for strong aberrations and/or multiple scattering background, to 4/9 in the ideal case [13]. The bias intensity can thus be rewritten as:

$$|\delta\mathcal{T}_{\rm in}(\mathbf{u})|^2 = \frac{1}{\mathcal{C}_{\rm out}^2 N_{\mathcal{W}}} \tag{38}$$

This last expression justifies the multi-scale analysis proposed in the accompanying paper. A gradual increase of the focusing quality, quantified by $\mathcal{C}$, is required to address smaller spatial windows that scale as $N_{\mathcal{W}}$. Following this scheme, the bias made of our $\mathbf{T}-$matrix estimator can be minimized and the iterative phase reversal algorithm converges towards a satisfying estimator.

D. Numerical validation of the iterative phase reversal process

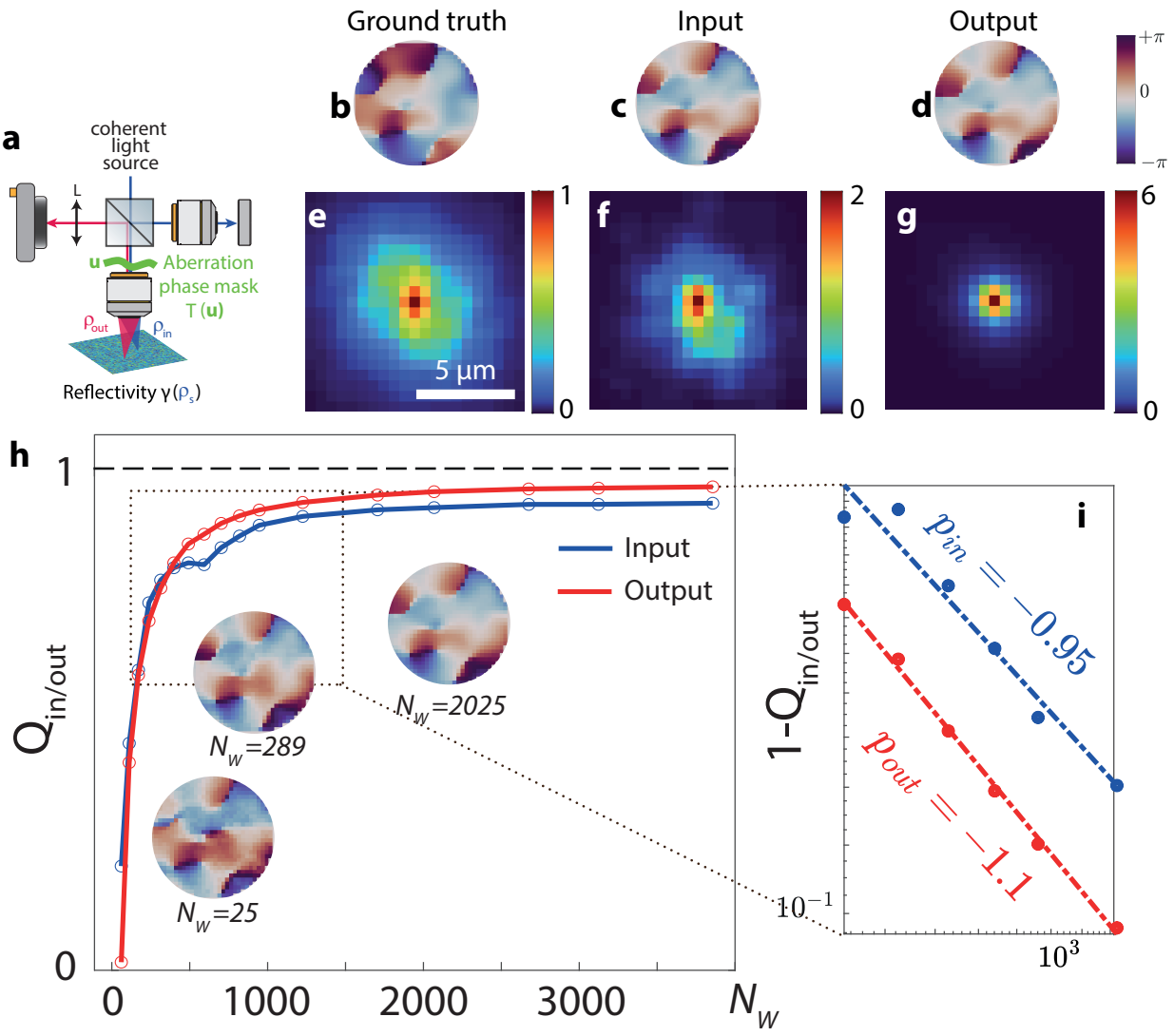
The IPR algorithm is now validated by means of a numerical simulation. The numerical simulation emulates an imaging experiment in an epi-detection configuration, as depicted in Supplementary Fig. 3a. The experimental conditions (numerical aperture, focal length, '*etc.*) are identical to our experiment. The field-of-view contains $N = 61 \times 61$ independent resolution cells. For sake of simplicity, a plane object of random complex reflectivity $\gamma(\boldsymbol{\rho})$ is considered in the focal plane of the microscope objective and the isoplanatic assumption is also made. Under these assumptions, the coefficients of the reflection matrix can be expressed in the pupil basis as follows:

$$R(\mathbf{u}_{\rm out}, \mathbf{u}_{\rm in}) = \mathcal{T}(\mathbf{u}_{\rm out})\tilde{\gamma}(\mathbf{u}_{\rm out} + \mathbf{u}_{\rm in})\mathcal{T}(\mathbf{u}_{\rm in}) \tag{39}$$

where $\tilde{\gamma}(\mathbf{u}) = \int d\boldsymbol{\rho}_s \gamma(\rho_s) \exp\left(2\pi \mathbf{u}\cdot\boldsymbol{\rho}_s/(\lambda f)\right)$, the Fourier transform of the sample reflectivity. The aberrations are thus modelled as a random phase screen of transmittance $\boldsymbol{\mathcal{T}}$. It exhibits a Gaussian statistics of correlation length $\ell_\phi = 2$ μm, and standard deviation $\sigma_\phi = 0.2$. The aberration phase law is displayed in Supplementary Fig. 3b. Once the reflection matrix $\mathbf{R_{uu}}$ is built in the pupil basis, a spatial Fourier transform yields the reflection matrix $\mathbf{R}_{\boldsymbol{\rho\rho}}$ in the focused basis, such that:

$$\mathbf{R}_{\boldsymbol{\rho\rho}} = \mathbf{T}_0^* \times \mathbf{R_{uu}}. \times \mathbf{T}_0^\dagger. \tag{40}$$

The resulting reflection matrix yields an estimate of the reflection point-spread function shown in Supplementary Fig. 3e. The distortion matrices $\mathbf{D}_{\rm in/out}$ in input and output are



SUPPLEMENTARY FIGURE 3. **Numerical validation of the iterative phase reversal algorithm**. **a.** Experimental configuration. Aberration are modelled by a random phase screen introduced in the pupil plane of the microscope objective. The object exhibits a random reflectivity. **b.** Simulated Gaussian random phase screen ($\sigma_\phi = 0.2$, $\ell_\phi = 2$ μm). **c-d.** Estimated input and output phase laws estimated by IPR ($N_\mathcal{W} = N^2 = 61^2$). **e.** Original RPSF before any correction. (scale bar: 5 μm). **f.** RPSF after aberration correction at input. **g** RPSF after correction at input and output. **h.** Scalar product $Q_{\text{in/out}}$ between the estimated aberration transmittance and its ground truth as a function of $N_\mathcal{W}$ (averaged over 10 realizations of disorder). The estimated aberration phase law is displayed for different values of $N_\mathcal{W}$ as insets. **i.** $(1 - Q_{\text{in/out}})$ as a function of $N_\mathcal{W}$ in log-log scale. Numerical points (disks) are fitted by linear curves (dashed lines).

derived from the matrix $\mathbf{R}$, as described in Supplementary Section 2 C, and the estimations of the input and output aberration transmittances $\hat{\mathcal{T}}_{\text{in/out}}(\mathbf{u}_{\text{in/out}})$ are computed using the IPR process described in the Methods section of the accompanying paper.

Supplementary Figures 3c and d show the estimated transmittances $\hat{\boldsymbol{\mathcal{T}}}_{\text{in/out}}$, respectively, when the whole FOV is considered. A strong similarity is observed with the ground truth up to a phase ramp [8] (Supplementary Fig. 3b). The corresponding RSPFs after each correction are displayed in Supplementary Figs. 3f and g. A diffraction-limited resolution is obtained at the end of the RMI process, which validates the IPR algorithm.

One can go further by investigating the convergence of the process as a function of N_W, the size of the spatial window considered for the computation of the correlation matrices $\mathbf{C}_{\text{in/out}}$. The similarity between the estimators $\hat{\boldsymbol{\mathcal{T}}}_{\text{in/out}}$ and the ground truth $\boldsymbol{\mathcal{T}}$ is evaluated by the normalized scalar product $Q_{\text{in/out}} = N_u^{-1}\hat{\boldsymbol{\mathcal{T}}}_{\text{in/out}} \times \boldsymbol{\mathcal{T}}^{\dagger}$, or, in terms of matrix coefficients.

$$Q_{\text{in/out}} = N_u^{-1}\sum_{\mathbf{u}} \hat{\mathcal{T}}_{\text{in/out}}(\mathbf{u})\mathcal{T}^{\star}(\mathbf{u}). \tag{41}$$

The evolution of Q_{in} and P_{out} is displayed as a function of N_W in Supplementary Fig. 3h. The convergence can be considered as fulfilled for $Q > 0.9$, *i.e* $N_{\mathcal{W}} \sim 500$, which is roughly the number of resolution cells contained in the final spatial windows ($L = 6$ μm) in our experiment.

This convergence rate is directly related to the bias of $\hat{\boldsymbol{\mathcal{T}}}_{\text{in/out}}$ (Eq. 38). To show it, let us first express the intensity bias $|\delta\mathcal{T}(\mathbf{u})|^2$ as a function of the phase error $\delta\phi(\mathbf{u})$ exhibited by the estimator $\hat{\mathcal{T}}(\mathbf{u})$ with respect to $\mathcal{T}(\mathbf{u})$, following the same formalism as in Supplementary Section 3 C:

$$|\delta\mathcal{T}(\mathbf{u})|^2 = |1 - \exp\left[i\delta\phi(\mathbf{u})\right]|^2 \underset{\delta\phi\ll 1}{\sim} |1 - (1+\delta\phi)|^2 \underset{\delta\phi\ll 1}{\sim} |\delta\phi|^2 \tag{42}$$

On the other hand, the scalar product as a function of the phase error $\delta\phi$ writes as such:

$$Q_{\text{in/out}} = N_u^{-1}\sum_{\mathbf{u}} \exp\left[i\delta\phi(\mathbf{u})\right] \tag{43}$$

The sum over the points in the Fourier plane $\mathbf{u}$ can be replaced by an ensemble average, since $N >> 1$:

$$Q_{\text{in/out}} = \langle \exp\left[i\delta\phi(\mathbf{u})\right] \rangle \tag{44}$$

Assuming a small phase error ($\delta\phi \ll 1$),

$$Q_{\text{in/out}} \sim 1 + i\,\langle\delta\phi\rangle - \frac{\langle(\delta\phi)^2\rangle}{2} \tag{45}$$

$$\sim 1 - \frac{\langle(\delta\phi)^2\rangle}{2} \tag{46}$$

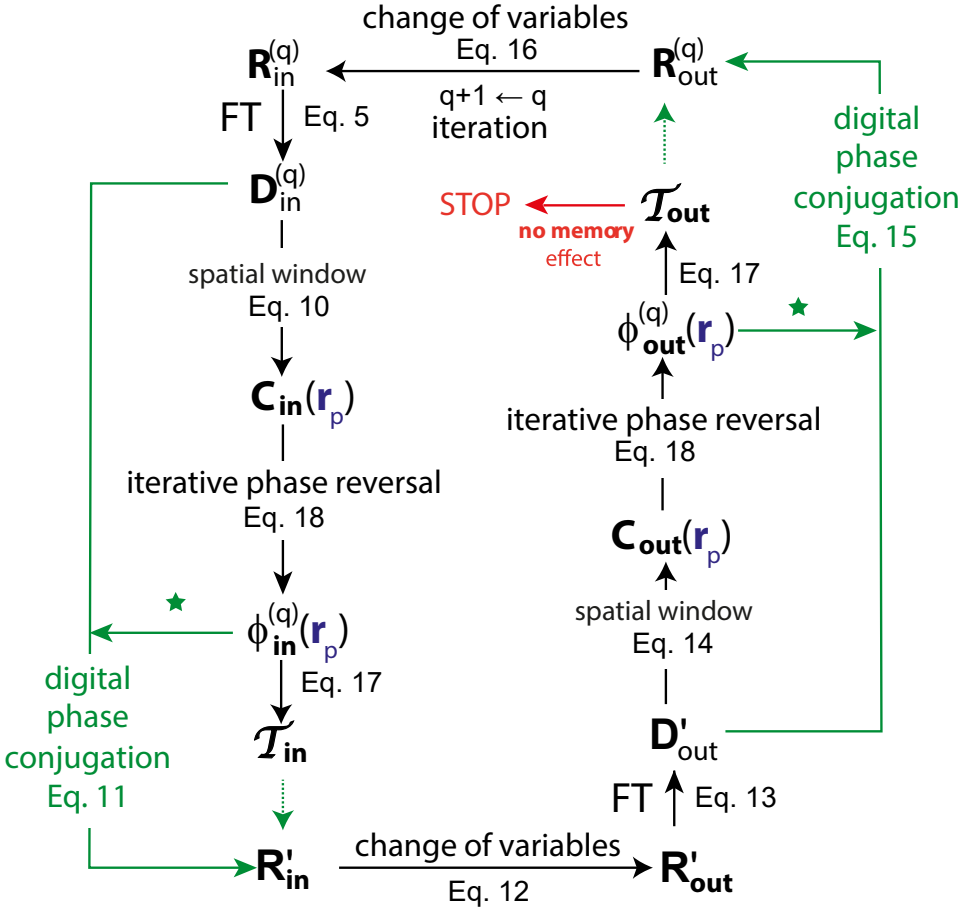
since $\langle\delta\phi\rangle = 0$. Combining this last expression with Eq. 42 leads to:

$$Q_{\text{in/out}} \sim 1 - \frac{\langle|\delta T|^2\rangle}{2} \tag{47}$$

According to Eq. 38, $1 - Q_{\text{in/out}}$ should therefore scale as the inverse of the number of independent resolution cells contained in the spatial window: $1 - P_{\text{in/out}} \propto N_{\mathcal{W}}^{-1}$. To highlight this scaling law, $1 - Q_{\text{in/out}}$ can be plotted in log-log scale as a function of $N_{\mathcal{W}}$ (Supplementary Fig. 3h). A slope p close to 1 is obtained both at input and output: $p_{in} = -0.95$ and $p_{out} = -1.1$, confirming that the bias on the aberration estimation scales with the inverse of the number of independent resolution cells in the field of view (Eq. 38). Another interesting observation is the lower bias observed at output in Supplementary Fig. 3h,i. Indeed, the first correction at input increases the coherence factor $\mathcal{C}_{\text{in}}$ and reduces the size of the virtual guide star when investigating wave distortions at output. This gain in focusing quality improves the sharpness of the estimator $\hat{\boldsymbol{\mathcal{T}}}$, as already highlighted by the scaling of $|\delta\mathcal{T}|^2$ as the inverse square of the coherence factor in Eq. 38.

In the present numerical simulation, the isoplanicity assumption makes the IPR algorithm converging towards an appropriate solution in one iteration at input and output. In the experiment, the situation is more complex since aberrations are spatially-distributed. In that case, an iterative compensation of wave distortions aver a multiple scale is required. The corresponding strategy is explained in the next Section.

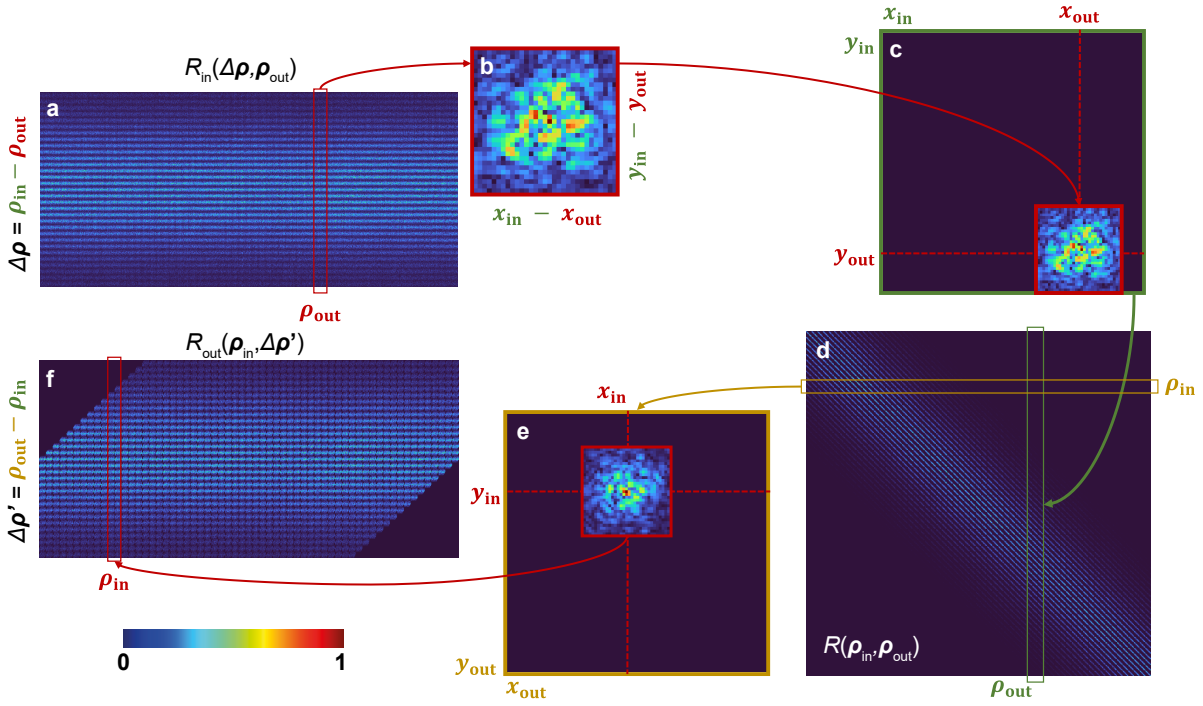
E. Multi-scale compensation of wave distortions



SUPPLEMENTARY FIGURE 4. **Flowchart of the multi-scale matrix imaging process.**

The multi-scale compensation of wave distortions consists in dividing by two the lateral extension L of the spatial windows $\mathcal{W}$ at each step. The full process is described in the Methods section of the accompanying paper and summarized in a flowchart displayed in Supplementary Fig. 4. At each step, the correction process is iterated both at input and output of the reflection matrix (left and right parts of Supplementary Fig. 4). Mathematically, the transfer between the input and output de-scanned bases is performed by a change of variable (Eqs. 12 and 16) illustrated by Supplementary Fig. 5. In particular, Supplementary Fig. 5f shows that the output de-scan matrix $\mathbf{R}_{\rm out}$ cannot be fully retrieved. A set of coefficients cannot be determined in its corners and are arbitrarily fixed to zero. They correspond to de-scanned coordinates $(\boldsymbol{\rho}_{\rm in}, \Delta\boldsymbol{\rho}')$ associated with points $\boldsymbol{\rho}_{\rm out} = \boldsymbol{\rho}_{\rm in} + \Delta\boldsymbol{\rho}'$ outside of the initial field-of-detection. To avoid the potential detrimental impact of such

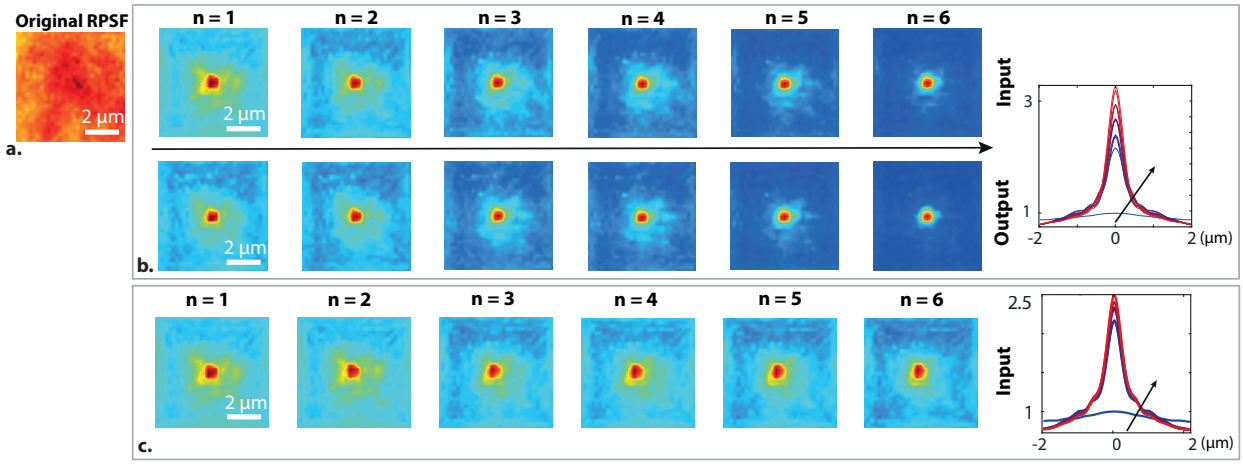
zero coefficients on the estimation of the $\boldsymbol{\mathcal{T}}-$matrix, the output correlation matrix $\mathbf{C}_{\text{out}}$ is only computed over points $\boldsymbol{\rho}_{\text{in}}$ that are associated with a full de-scan wave-field, *i.e* points $\boldsymbol{\rho}_{\text{in}}$ such that $R_{\text{out}}(\boldsymbol{\rho}_{\text{in}}, \Delta\boldsymbol{\rho}') \neq 0$ for each de-scan position $\Delta\boldsymbol{\rho}'$.



SUPPLEMENTARY FIGURE 5. **Conversion of the reflection matrix from the input to the output de-scanned basis. a.** Reflection matrix $\mathbf{R}_{\text{in}}$ in the input de-scanned basis. **b.** Each column reshaped in 2D corresponds to the input focal spot de-scanned with respect to the output focusing point $\boldsymbol{\rho}_{\text{out}}$. **c-d.** Each focal spot can be re-expressed in the laboratory frame ($\boldsymbol{\rho}_{\text{in}}$) (**c**) and stored in the canonical reflection matrix $\mathbf{R}$ (**d**). **e.** Each line of $\mathbf{R}$ can be reshaped in 2D corresponds to the output focal spot in the focused basis ($\boldsymbol{\rho}_{\text{out}}$). **f.** Each output focal spot can be de-scanned with respect to the input focusing point $\boldsymbol{\rho}_{\text{in}}$ and stored in the output de-scan matrix $\mathbf{R}_{\text{out}}$.

In a previous work [6], the compensation of wave-front distortions was performed in one single step and on a single side (output). The low spatial sampling of the reflection matrix at input explained this minimalist strategy. In the accompanying paper, the de-scanned measurement of the reflection matrix provides the same sampling of the wave-field at input and output. An alternate compensation of wave distortions is therefore possible and actually critical if one wants to converge towards a sharp estimator of the $\boldsymbol{\mathcal{T}}$-matrix. Indeed, as shown

by Eq. 38, the bias of this estimator on one side (input/output) directly depends on the focusing quality on the other side (output/input) since it controls the blurring of the virtual guide star synthesized by a coherent combination of focal spots. By alternating aberration compensation at input and output, we can improve gradually the coherence factor $\mathcal{C}_{\text{out/in}}$ and address forward multiple scattering associated with smaller isoplanatic patches (decrease $N_{\mathcal{W}}$) while maintaining the bias $\delta\mathcal{T}_{\text{in/out}}$ at a sufficiently low level.



SUPPLEMENTARY FIGURE 6. **On the importance of alternating the compensation of wave distortions at input and output. a.** Original RPSF at the same position considered in Fig. 5 of the accompanying paper ($z = 200$ μm). **b.** Local RPSF at the same position, after every step of the iterative process (multi-scale and input/output). **c**. Local RPSF at the same position, after every step of the iterative process (multi-scale and input only). For panels **b** and **c**, the evolution of the radial profile of the RPSF throughout the iterative process is displayed on the right. Sacle bar: 2μm.

Supplementary Figure 6 illustrates the importance of an alternate compensation of aberration and scattering at input and output. Supplementary Figure 6b shows the evolution of the RPSF at each step of the algorithm when balancing between input and output. Supplementary Figure 6c shows the evolution of the RPSF when the algorithm is only iterated at input. While a continuous balance between input and output aberration phase laws allows us to reach a diffraction-limited resolution at the end of the process (Fig.R3b), the absence of correction at output prevents from a refinement of the virtual guide star and does not allow our algorithm to converge towards a satisfying estimation of the matrix $\boldsymbol{\mathcal{T}}_{\text{in}}$.

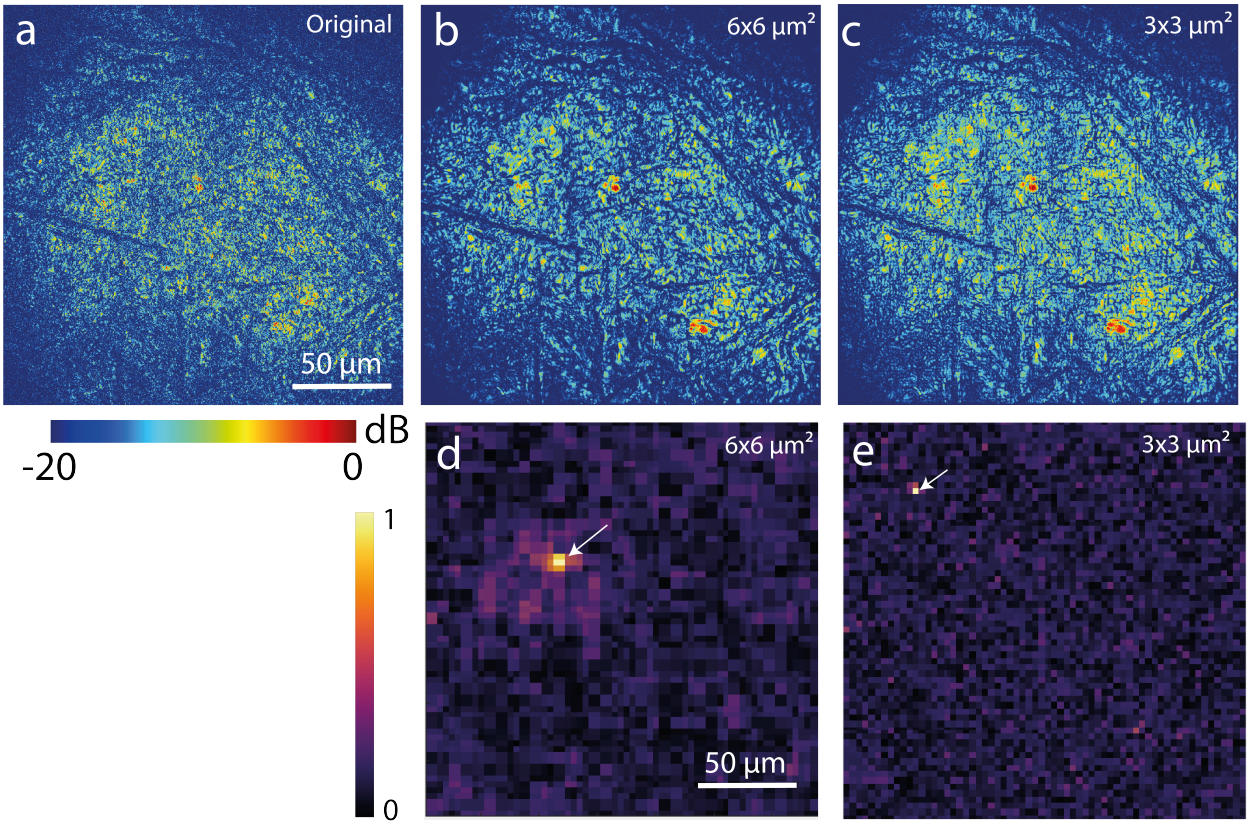
F. Convergence of the multi-scale analysis process

The multi-scale process shown in Fig. 4 shall be stopped at some iterative step. Indeed, the spatial window W_L cannot be reduced to a speckle grain otherwise the method would lead to a bucket image that consists in an incoherent summation of each de-scanned wave-field. Qualitatively, the end of the process can be determined by a careful look at the image. An incoherent compensation of aberrations induces a loss of contrast on the final image. Figure 7 illustrates this assertion by comparing the original image (Fig. 7a), the RMI image obtained with a $\boldsymbol{\mathcal{T}}-$matrix of optimal resolution (6×6 μm^2, see Supplementary Fig. 7b) and a RMI image based on too small spatial windows W_L (3×3 μm^2, see Supplementary Fig. 7c). The contrast of each image $I(\boldsymbol{\rho}, z)$, $\mathcal{F}(z) = \mathrm{std}\left[I(\boldsymbol{\rho}, z)\right] / \langle I(\boldsymbol{\rho}, z)\rangle$, tends to gradually increase when the estimator $\hat{\boldsymbol{\mathcal{T}}}$ approaches $\boldsymbol{\mathcal{T}}$ (see comparison between Supplementary Figs. 7a and b) and decrease when the compensation of aberrations and scattering becomes bucket-like (see comparison between Supplementary Figs. 7b and c). For the images displayed in Supplementary Figs. 7a, b and c, we find $\mathcal{F} \sim 1.48$, $\mathcal{F} \sim 1.61$ and $\mathcal{F} \sim 1.37$, respectively. Nevertheless, an optimization criterion only based on the image contrast can be misleading since the contrast also depends on the sample reflectivity distribution.

A more reliable observable is the spatial correlation function $C_S(\mathbf{r}_\mathrm{p}, \mathbf{r}'_\mathrm{p})$ of the scattering component of the $\boldsymbol{\mathcal{T}}-$matrix between neighboring points $\mathbf{r}_\mathrm{p}$ and $\mathbf{r}'_\mathrm{p}$ (Methods). Examples of this spatial correlation function are displayed in Supplementary Figs. 7d and 7e. While a spatial window of 6×6 μm^2 preserves a short-range correlation between neighbor windows (Supplementary Fig. 7d), a spatial window of 3×3 μm^2 leads to a fully spatially incoherent estimator $\hat{\boldsymbol{\mathcal{T}}}$ (Supplementary Fig. 7e). This observable clearly shows whether the estimator $\hat{\boldsymbol{\mathcal{T}}}$ leads to a coherent (i.e physical) or incoherent (i.e bucket-like) compensation of scattering. The number of iterations in the phase reversal algorithm has thus been based on this $\boldsymbol{\mathcal{T}}-$matrix correlation criterion.

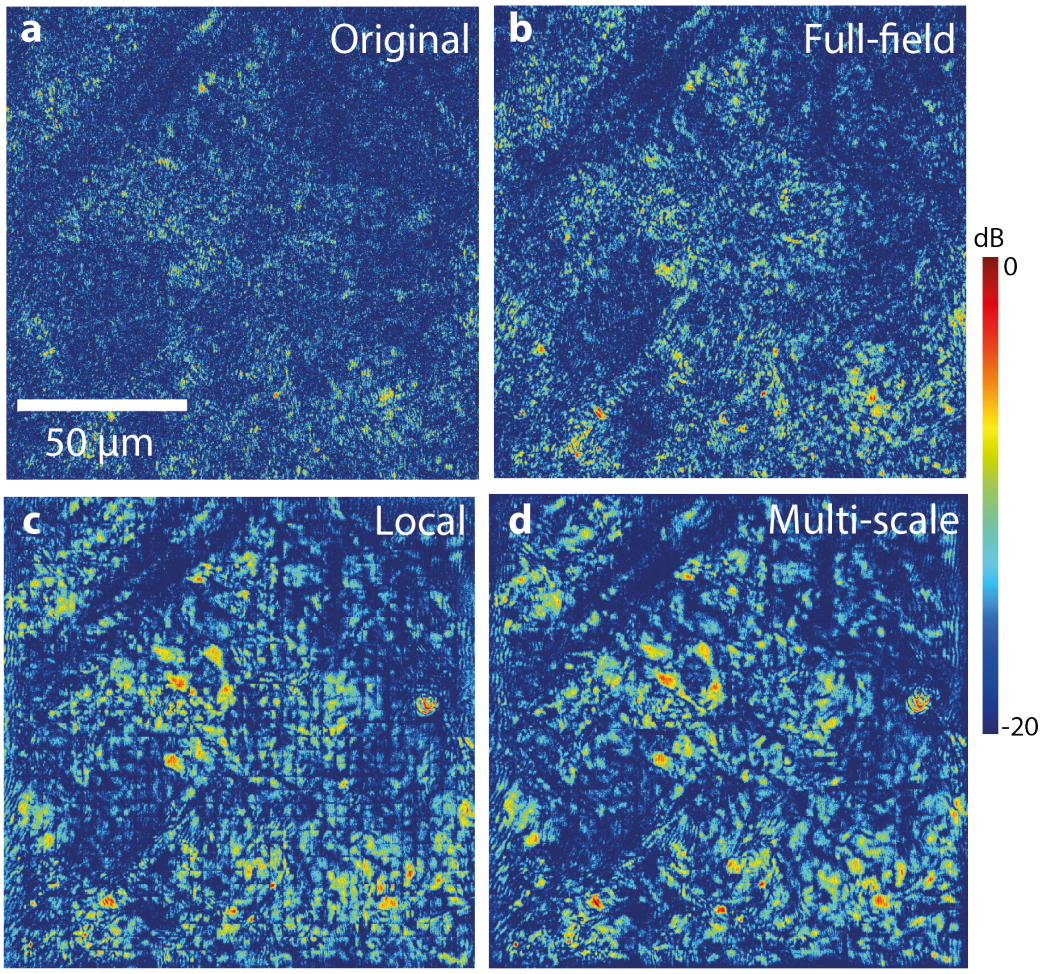
G. Benefit of a multi-scale strategy

Supplementary Figure 8 shows the benefit of a multi-scale compensation of wave distortions. On the one hand, a full-field correction only addresses the aberrations induced by the reference arm and does not address forward multiple scattering (Supplementary Section 4 D). It thus



SUPPLEMENTARY FIGURE 7. **Confocal images at several steps of the multi-scale analysis**. **a.** Initial en-face image of the cornea at depth $z \sim 100$ μm. **b-c.** RMI images based on a $\boldsymbol{\mathcal{T}}-$matrix estimator of spatial resolution $L = 6$ μm and $L = 3$ μm, respectively. **d-e.** Spatial correlation $C_{\mathcal{S}}$ of $\boldsymbol{\mathcal{S}}$ with respect to one reference location (white arrow). Scale bars: 50 μm.

only provides a blurred view of the corneal internal structure (Supplementary Fig. 8b). On the other hand, a direct compensation of wave distortions leads to a strong vigneting effect (Supplementary Fig. 8c). The latter phenomenon is due to the imperfect convergence of the IPR algorithm over extremely reduced spatial windows (Supplementary Sec. 3 C). Note that this detrimental effect is not limited to IPR but also exists for other algorithms such as CLASS (Supplementary Fig. $22b_1$) or ITR (Supplementary Fig. $19b_3$). On the contrary, our multi-scale strategy limits the bias of our estimator and provides a clear view of the cornea reflectivity without being hampered by any vignetting phenomenon.



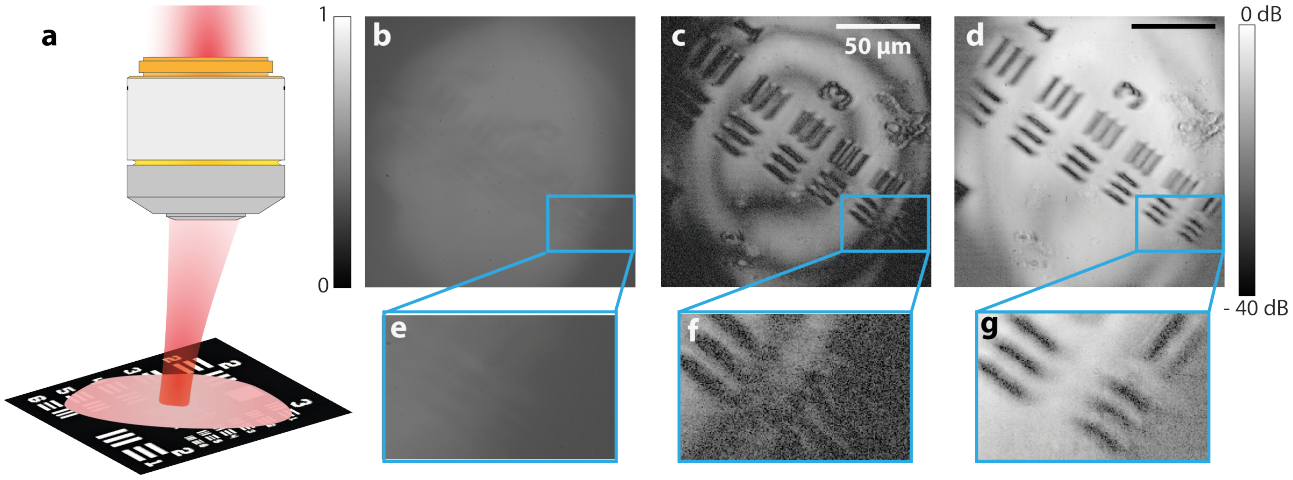
SUPPLEMENTARY FIGURE 8. **On the importance of a multi-scale compensation of wave distortions. a.** Original confocal image of the cornea at $z = 200$ μm. **b.** Full-field correction. **c.** Direct compensation of aberrations over reduced spatial windows ($L = 6$ μm). **d.** Multi-scale strategy. Scale bar: 50 μm

H. Validation of the method with a ground-truth object

We now provide an experimental validation of the method using a resolution target behind the scattering medium. Although such a specular object does not reproduce the reflectivity properties of tissues, this reference experiment will allow us to validate our multi-scale analysis of wave distortions and also outline its limits.

This experiment is displayed in Supplementary Fig. 9. It consists in the imaging of a resolution target placed right behind a 500-μm-thick mouse peritoneum layer (Supplementary

Fig. 9a). This tissue layer roughly displays the same scattering properties as the cornea used in the accompanying manuscript.



SUPPLEMENTARY FIGURE 9. **Imaging a resolution target hidden behind an opaque tissue layer. a.** Experimental configuration. Image credit: Setreset on Wikimedia Commons (https://creativecommons.org/licenses/by-sa/3.0/deed.en). **b.** Incoherent image (colorbar in linear scale). **c.** FFOCT image (B&W bar in log-scale). **d.** Matrix Image (B&W bar in log-scale). **e-h.** Zooms on the smallest details of the resolution target images displayed in panels **b-d**, respectively. Scale bar: 50 μm.

Supplementary Figure 9b displays the incoherent image of the target in reflection which is obtained here by blocking the reference arm in the experimental set up. Its foggy feature highlights the strong turbidity of the scattering layer. Supplementary Figure 9c shows the FFOCT image acquired for $\Delta\boldsymbol{\rho}_{\text{in}} = \mathbf{0}$. Its comparison with Supplementary Fig. 9b illustrates the drastic filtering of diffuse multiple scattering operated by the time gating process in FFOCT. It also shows how the confocal filter allows to reveal the large patterns of the resolution target. The fact that FFOCT is robust with respect to aberrations for specular objects has already been noticed in a previous work [5]. In that case, aberrations only give rise to fluctuations of image contrast across the field-of-view. Nevertheless, this robustness to aberrations vanishes for the smallest details of the target that cannot be detected [see the corresponding zoom in Supplementary Fig. 9g].

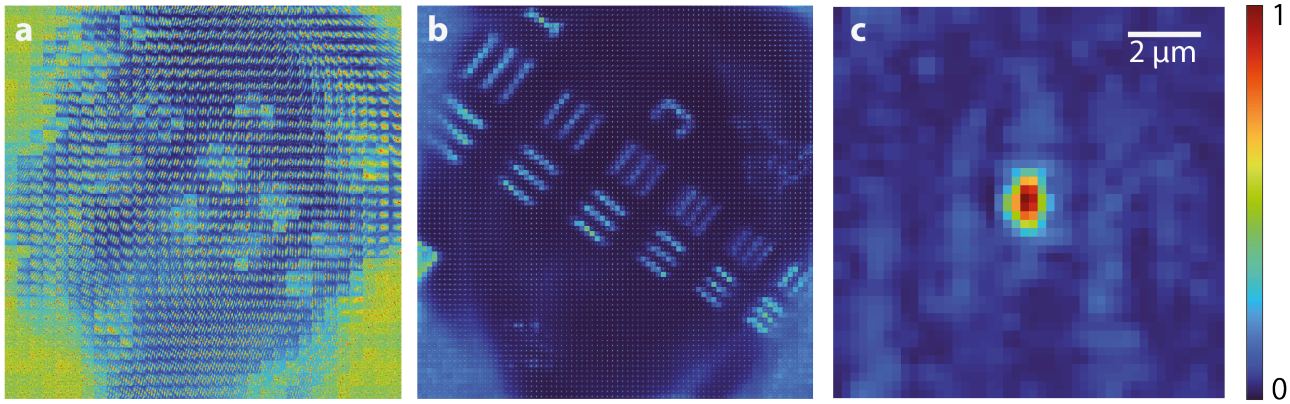
The aberration and scattering induced by the tissue layer can be evaluated by the RPSF whose spatial evolution is displayed in Supplementary Fig. 10a. It shows drastic variations across the field-of-view, a manifestation of a particularly short-range memory effect across the field-of-view. Compared with the incoherent RPSFs measured inside the cornea (Fig. 4b of the accompanying paper), the coherent RPSFs here show a more contrasted feature. This is due to the specular nature of the sample. In that regime, the RPSF is a coherent function of the focusing quality since it scales as the convolution between the coherent input and output PSFs [14]:

$$I(\Delta\boldsymbol{\rho}_{\text{in}}, \boldsymbol{\rho}_{\text{out}}, z) = |H_{\text{in}}^{(l)} \overset{\Delta\boldsymbol{\rho}_{\text{in}}}{\circledast} H_{\text{out}}^{(l)}(\Delta\rho_{\text{in}}, \boldsymbol{\rho}_{\text{out}}, z)|^2.$$

On the contrary, for a sample of random reflectivity (like the opaque cornea under study), the RPSF is an incoherent measure of the focusing quality. Its ensemble average can be expressed as the convolution between the incoherent input and output PSFs (Eq. 3 of the accompanying paper):

$$\langle I(\Delta\boldsymbol{\rho}_{\text{in}}, \boldsymbol{\rho}_{\text{out}}, z)\rangle \propto |H_{\text{in}}^{(l)}|^2 \overset{\Delta\boldsymbol{\rho}_{\text{in}}}{\circledast} |H_{\text{out}}^{(l)}|^2(\Delta\boldsymbol{\rho}_{\text{in}}, \boldsymbol{\rho}_{\text{out}}, z).$$

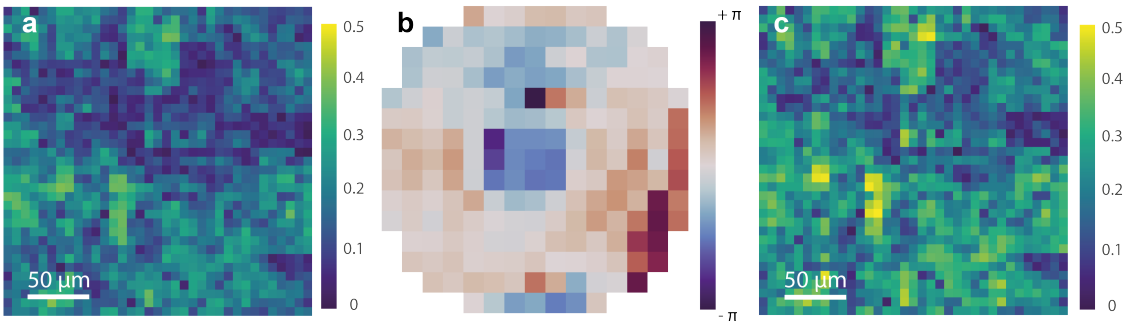
Despite the short-range memory effect highlighted by the original RPSFs (Supplementary Fig. 10a), a multi-scale compensation of aberration and scattering phenomena allows us to retrieve an almost diffraction-limited RPSF across the whole surface (Supplementary Fig. 10b), except inside the patterns of the resolution target since there is no back-scattered wave-field there. The resulting image is displayed in Supplementary Fig. 9d. Compared with its original counterpart (Supplementary Fig. 9c), an homogeneous contrast is obtained throughout the field-of-view. Above all, RMI is able to retrieve the smallest details of the resolution target (Supplementary Fig. 9g) that FFOCT initially failed to reveal (Supplementary Fig. 9f). Nevertheless, the image is not perfect. A first reason comes from the limited de-scan of the RPSF. This loss of information gives rise to a residual incoherent background in the final RPSF (Supplementary Fig. 10c). The second reason is the limited isoplanicity. The size L of spatial windows at the end of the RMI process is limited to 10 μm. Hence we cannot compensate for scattering phenomena giving rise to a memory effect range smaller than L.



SUPPLEMENTARY FIGURE 10. **Reflection point spread function in the resolution target experiment.**. **a.** Map of initial RPSFs. **b.** Map of final RPSFs. **c.** Mean RPSF after aberration compensation (scale bar: 2 μm).

4. ANALYSIS OF THE TRANSMITTANCE MATRIX

A. Discrepancy between input and output $\mathcal{T}-$matrices



SUPPLEMENTARY FIGURE 11. **Discrepancy between input and output T−matrices. a.** Scalar product $P(\boldsymbol{\rho}_\mathrm{p}, z)$ between $\hat{\boldsymbol{\mathcal{T}}}_\mathrm{in}$ and $\hat{\boldsymbol{\mathcal{T}}}_\mathrm{out}$ at depth z =200 μm. **b.** Phase of the first pupil singular vector $\mathbf{U}_1$ of $\hat{\boldsymbol{\mathcal{T}}}_\mathrm{in}$. **c.** Scalar product $P'(\boldsymbol{\rho}_\mathrm{p}, z)$ between $\hat{\boldsymbol{\mathcal{T}}}'_\mathrm{in}$ and $\hat{\boldsymbol{\mathcal{T}}}_\mathrm{out}$. Scale bar: 50 μm.

While spatial reciprocity implies a strict equality between the wave distortions undergone by the incident and reflected waves in the sample arm of our experimental set-up, the input and output estimators of the $\boldsymbol{\mathcal{T}}-$matrix are far from it (see Figs. 4e and f of the accompanying paper). This discrepancy can be quantified by computing the normalized scalar product $P(\boldsymbol{\rho}_\mathrm{p}, z)$ between the coefficients of $\hat{\boldsymbol{\mathcal{T}}}_\mathrm{in}$ and $\hat{\boldsymbol{\mathcal{T}}}_\mathrm{out}$:

$$P(\boldsymbol{\rho}_\mathrm{p}, z) = N_u^{-1} \sum_{\mathbf{u}} \hat{\mathcal{T}}_\mathrm{in}(\mathbf{u}, \boldsymbol{\rho}_\mathrm{p}, z) \hat{\mathcal{T}}^*_\mathrm{out}(\mathbf{u}, \boldsymbol{\rho}_\mathrm{p}, z) \tag{48}$$

Supplementary Fig. 11 shows the transverse evolution of this scalar product at depth $z = 200$ μm. As it could be anticipated when looking at the $\hat{\boldsymbol{\mathcal{T}}}-$matrices in Figs. 4e and f, this scalar product is quite low: $P(\boldsymbol{\rho}_\mathrm{p}, z) = 0.3$ in average. As we will see, this discrepancy can be, at least partially, explained by the aberrations in the reference arm. Indeed, according to Eq. 8, the input transmission matrix accumulates the aberrations undergone by the incident wave-field in the sample arm and the aberrations undergone by the reference wave-field,

$$\boldsymbol{\mathcal{T}}_\mathrm{in} = \boldsymbol{\mathcal{T}} \circ \boldsymbol{\mathcal{T}}_\mathrm{ref}. \tag{49}$$

On the contrary, $\hat{\boldsymbol{\mathcal{T}}}_\mathrm{out}$ only grasps the wave distortions undergone by the reflected wave-field in the sample arm. If, in a first approximation, we assume that the aberration due to the

reference arm is isoplanatic, it can be extracted by considering the first eigenstate of $\hat{\boldsymbol{\mathcal{T}}}_{\text{in}}$ (see Supplementary Section 4 B). The phase of the pupil singular vector $\mathbf{U}_1$ displayed in Supplementary Fig. 11 is an estimator of $\boldsymbol{\mathcal{T}}_{\text{ref}}$. Not surprisingly, it mainly corresponds to a spherical aberration phase law. One can subtract this reference phase to $\hat{\boldsymbol{\mathcal{T}}}_{\text{in}}$ in order to build a matrix $\hat{\boldsymbol{\mathcal{T}}}'_{\text{in}} = \hat{\boldsymbol{\mathcal{T}}}_{\text{in}} \circ \mathbf{U}_1^*$. One can expect the scalar product $P'(\boldsymbol{\rho}_p, z)$ between $\hat{\boldsymbol{\mathcal{T}}}'_{\text{in}}$ and $\hat{\boldsymbol{\mathcal{T}}}_{\text{out}}$ to be increased compared to its initial value $P(\boldsymbol{\rho}_p, z)$ (see comparison between Supplementary Figs. 11a and c). This is actually what we observe even though the scalar product P' remains smaller than 0.7 (Supplementary Fig. 11c). It means that the spherical aberration law induced by the reference arm account partially for the mismatch between $\hat{\boldsymbol{\mathcal{T}}}_{\text{in}}$ and $\hat{\boldsymbol{\mathcal{T}}}_{\text{out}}$.

The residual mismatch can be explained by the fact that the aberration induced by the reference arm is not strictly isoplanatic. Misalignment between sample and reference arms manifests as a transverse shift of the RPSF that varies across the field-of-view as illustrated by Fig.4c. Field curvature can also induce spatially-varying aberrations that our approach can address but they are difficult to discriminate from sample arm aberrations. Last but not least, another phenomenon that can contribute to this discrepancy between input and output aberration phase laws is the bias of our $\boldsymbol{\mathcal{T}}$-matrix estimator, especially for small spatial windows L as explained in Supplementary Section 3 C.

B. Aberration and scattering components of the $\mathcal{T}-$matrix

In a previous work, Badon *et al.* showed how the singular value decomposition (SVD) of the $\mathbf{D}-$matrix provided a decomposition of the field-of-view into isoplanatic modes in the case of a specular object. In the present paper, this property does not hold since we cope with a random distribution of heterogeneities. In this regime, this is the SVD of the $\boldsymbol{\mathcal{T}}$-matrix estimator that enables a mapping of isoplanatic modes. As recently shown in an ultrasound study [8], the complexity of the associated aberration phase laws increases with the rank of the corresponding singular values while the spatial extension of the isoplanatic mode decreases. As we will show below, this complexity can be quantified by a vorticity degree of the associated transmittance, quantity that has a direct link with the occurrence of multiple scattering paths involved in the trajectory of the wave from the focal plane to the camera sensors.

The SVD of $\hat{\boldsymbol{\mathcal{T}}}$ writes:

$$\hat{\boldsymbol{\mathcal{T}}} = \sum_k \sigma_k \mathbf{U}_k \mathbf{V}_k^\dagger \tag{50}$$

where σ_k are the singular values arranged in decreasing order. $\mathbf{U}_k = [U_k(\mathbf{u})]$ and $\mathbf{V}_k = [V_k(\boldsymbol{\rho}_\mathrm{p})]$ are the singular vectors of $\hat{\boldsymbol{\mathcal{T}}}$ in the pupil and focal plane, respectively. For a physical interpretation of these vectors, we take advantage of the equivalence between the SVD of $\hat{\boldsymbol{\mathcal{T}}}$ and the eigenvalue decomposition of the spatial correlation matrix,

$$\mathbf{C}_\mathcal{T} = \hat{\boldsymbol{\mathcal{T}}} \times \hat{\boldsymbol{\mathcal{T}}}^\dagger. \tag{51}$$

The elements of $\mathbf{C}_\mathcal{T}$ correspond to the correlation coefficients between aberration phase laws obtained for each image pixel $\boldsymbol{\rho}_p$ and $\boldsymbol{\rho}'_p$:

$$C_\mathcal{T}(\boldsymbol{\rho}_p, \boldsymbol{\rho}'_p) = \sum_{\mathbf{u}} \hat{\mathcal{T}}(\mathbf{u}, \boldsymbol{\rho}_p) \hat{\mathcal{T}}^*(\mathbf{u}, \boldsymbol{\rho}_p). \tag{52}$$

The first eigenvector $\mathbf{V}_1$ of $\mathbf{C}_\mathcal{T}$ is thus the spatial domain where the degree of correlation between aberration phase laws is maximized. This degree of correlation is quantified by the normalized eigenvalue $\overline{\sigma}_1^2$, such that

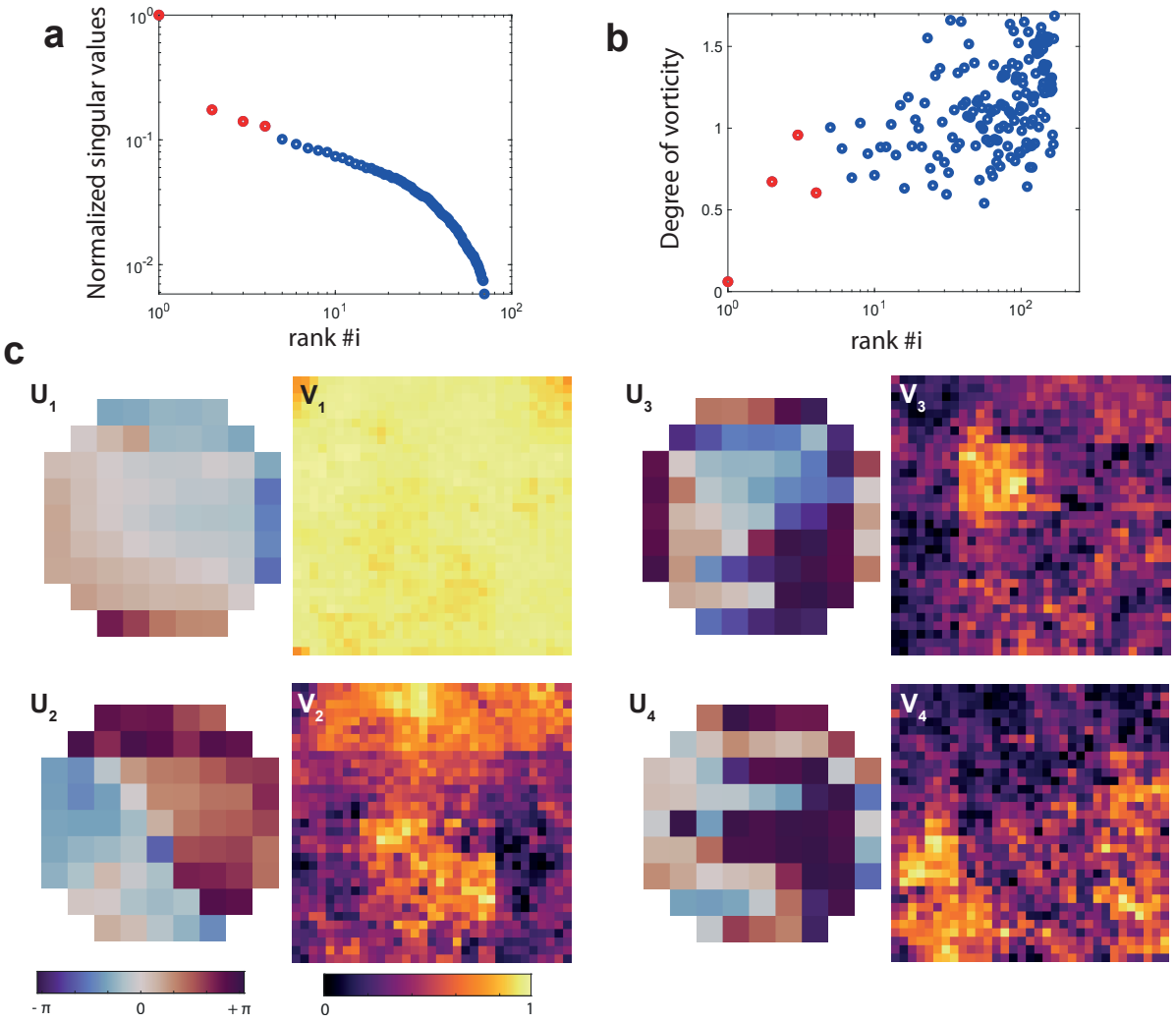
$$\overline{\sigma}_k^2 = \frac{\sigma_k^2}{\sum_l \sigma_l^2} = \frac{\mathbf{V}_k^\dagger \times \mathbf{C}_\mathcal{T} \times \mathbf{V}_k}{\mathrm{Tr}\{\mathbf{C}_\mathcal{T}\}} \tag{53}$$

The corresponding singular vector

$$\mathbf{U}_1 = \sigma_1^{-1} \hat{\boldsymbol{\mathcal{T}}} \times \mathbf{V}_1 \tag{54}$$

is the transmittance the most-spatially invariant across the field-of-view. The same process can be iterated on the matrix $\hat{\boldsymbol{\mathcal{T}}} - \sigma_1 \mathbf{U}_1 \times \mathbf{V}_1^\dagger$ to retrieve the second eigenstate and so on. A set of orthogonal isoplanatic modes $\mathbf{V}_k$ is finally obtained with a degree of correlation $\overline{\sigma}_k^2$ that decreases with their rank.

Supplementary Figure 12 shows the result of the SVD of $\hat{\boldsymbol{\mathcal{T}}}_\mathrm{out}$ for $z = 50$ μm (same depth as the one considered on top of Fig.6 of the accompanying paper). Supplementary Figure 12a displays its normalized singular values. A few predominant eigenvalues associated with the main isoplanatic modes seem to emerge from a continuum of lower eigenvalues associated with a multiple scattering background in each case. Supplementary Figure 12c shows the four first eigenstates of $\hat{\boldsymbol{\mathcal{T}}}_\mathrm{out}$. While the first eigenstate $\mathbf{V}_1$ spans over the whole field-of-view, the higher order isoplanatic modes $\mathbf{V}_k$ are associated with spatial domains whose size decrease



SUPPLEMENTARY FIGURE 12. **Singular value decomposition of the $\hat{\mathcal{T}}-$matrix at depth $z = 50$ μm. a.** Normalized singular values of $\hat{\mathcal{T}}_{\text{out}}$. **b.** Degree of vorticity associated with each pupil singular vector $\mathbf{U}_k$ of $\hat{\mathcal{T}}_{\text{out}}$. **c.** Four first eigenstates of $\hat{\mathcal{T}}_{\text{out}}$: Phase of the transmittance $\mathbf{U}_k$ and modulus of the corresponding isoplanatic modes $\mathbf{V}_k$.

with the rank k of the eigenstate. The complexity (i.e the spatial frequency content) of the associated transmittance $\mathbf{U}_k$ also increases with this rank.

The nature of the associated wave distortions can be investigated by considering the phase ϕ_k of each singular vector $\mathbf{U}_k$. More precisely, recent works [15, 16] showed how aberrations and scattering can be discriminated by computing the divergence and curl of the phase gradient $\nabla\phi_k$. Each phase law ϕ_k can be decomposed into: (i) an irrotational component $\phi_k^{(\text{irr})}$, such that $\nabla \wedge \nabla\phi_k^{(\text{irr})} = \mathbf{0}$, associated with low-order aberrations; (ii) a curl component

$\phi_k^{(\mathrm{rot})}$, such that $\nabla \cdot \nabla \phi_k^{(\mathrm{rot})} = 0$, induced by forward multiple scattering trajectories. Indeed, this curl component is a manifestation of optical vortices that necessarily originate from, at least, three interfering beams and thus suppose several optical trajectories, hence multiple scattering. A degree α of vorticity can be assessed by looking at the ratio between the energy of each contribution, such that:

$$\alpha_k = \frac{|\nabla \wedge \nabla \phi_k|^2}{|\Delta \phi_k|^2} \tag{55}$$

This degree of vorticity is displayed for each eigenstate in Supplementary Fig. 12b. Although it shows some fluctuations, α_k tends to increase with the rank k of eigenstate. It thus seems to indicate that the higher order eigenstates associated with smaller isoplanatic patches also exhibit a higher degree of vorticity, which can be a manifestation of forward multiple scattering paths.

C. Angular decomposition of the $\mathcal{T}$-matrix

To investigate the effect of forward multiple scattering, an angular decomposition of the transmitted wave-field between the cornea surface and the focal plane can be performed. Interestingly, this can be done by considering the Fourier transform of the transmission matrix estimator $\hat{\boldsymbol{\mathcal{T}}}(z) = [\hat{\mathcal{T}}(\mathbf{u}_{\mathrm{in}}, \boldsymbol{\rho}_{\mathrm{out}}, z)]$ along the focused basis:

$$\tilde{\boldsymbol{\mathcal{T}}}(z) = \hat{\boldsymbol{\mathcal{T}}}(z) \times \mathbf{T}_0, \tag{56}$$

which writes, in terms of matrix coefficients,

$$\tilde{\mathcal{T}}(\mathbf{u}, \Delta\mathbf{u}, z) = \sum_{\boldsymbol{\rho}_{\mathrm{out}}} \hat{\mathcal{T}}](\mathbf{u}_{\mathrm{in}}, \boldsymbol{\rho}_{\mathrm{out}}, z) \exp\left(-i\frac{2\pi}{\lambda f}\boldsymbol{\Delta}\mathbf{u}.\boldsymbol{\rho}_{\mathrm{out}}\right). \tag{57}$$

To show the relationship between $\tilde{\mathcal{T}}(\mathbf{u}_{\mathrm{in}}, \Delta\mathbf{u}, z)$ and the angular distribution of light in the focal plane, one can use the relationship between the transmission and transmittance matrices,

$$\mathbf{T} = \boldsymbol{\mathcal{T}} \circ \mathbf{T}_0, \tag{58}$$

which writes in terms of matrix coefficients:

$$T(\mathbf{u}_{\mathrm{in}}, \boldsymbol{\rho}_{\mathrm{out}}, z) = \mathcal{T}(\mathbf{u}_{\mathrm{in}}, \boldsymbol{\rho}_{\mathrm{out}}, z) \exp\left(j\frac{2\pi}{\lambda f}\mathbf{u}_{\mathrm{in}} \cdot \boldsymbol{\rho}_{\mathrm{out}}\right), \tag{59}$$

or, equivalently,

$$\mathcal{T}(\mathbf{u}_{\mathrm{in}}, \boldsymbol{\rho}_{\mathrm{out}}, z) = T(\mathbf{u}_{\mathrm{in}}, \boldsymbol{\rho}_{\mathrm{out}}, z) \exp\left(-j\frac{2\pi}{\lambda f}\mathbf{u}_{\mathrm{in}} \cdot \boldsymbol{\rho}_{\mathrm{out}}\right). \tag{60}$$

Injecting this last expression into Eq. 58 leads to the following expression for $\tilde{\mathcal{T}}$:

$$\tilde{\mathcal{T}}(\mathbf{u}_{\text{in}}, \Delta\mathbf{u}, z) = \sum_{\Delta\mathbf{u}} \exp\left[-j\frac{2\pi}{\lambda f}(\Delta\mathbf{u} + \mathbf{u}_{\text{in}}) \cdot \boldsymbol{\rho}_{\text{out}}\right] T(\mathbf{u}_{\text{in}}, \boldsymbol{\rho}_{\text{out}}) \tag{61}$$

$$= \tilde{T}(\mathbf{u}_{\text{in}}, \mathbf{u}_{\text{in}} + \Delta\mathbf{u}). \tag{62}$$

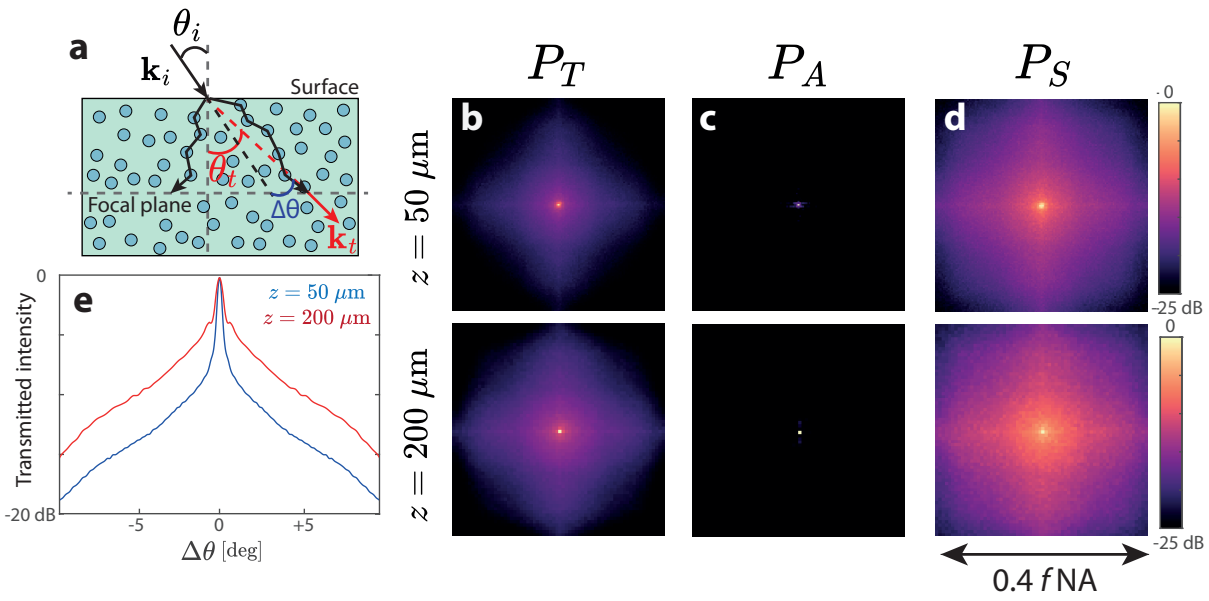
Hence, the $\tilde{\boldsymbol{\mathcal{T}}}-$matrix actually corresponds to the de-scan transmission matrix in the pupil plane. Its coefficients $\tilde{\mathcal{T}}(\mathbf{u}_{\text{in}}, \Delta\mathbf{u}, z)$ provide the angular dispersion of the transmitted wave-field at depth z with respect to the incident plane wave of transverse wave vector $\mathbf{k}_{\text{in}} = \mathbf{u}_{\text{in}}/f$ (Supplementary Fig. 13a). For small angles, the deviation angle $\Delta\boldsymbol{\theta} = (\Delta\theta_x, \Delta\theta_y)$ can be expressed as follows:

$$\Delta\boldsymbol{\theta} \sim \sin\boldsymbol{\theta}_{\text{out}} - \sin\boldsymbol{\theta}_{\text{in}} = \Delta\mathbf{u}/f \tag{63}$$

The angular dispersion of the wave-field between the cornea surface and the focal plane can thus be obtained by averaging the intensity of the transmitted wave-field over the incident wave vector:

$$P_{\mathcal{T}}(\Delta\mathbf{u}, z) = \left\langle |\tilde{\mathcal{T}}(\mathbf{u}_{\text{in}}, \Delta\mathbf{u}/f, z)|^2 \right\rangle_{\mathbf{u}_{\text{in}}}. \tag{64}$$

Supplementary Figure 13b shows this angular distribution at depths $z = 50$ and 200 μm, respectively. It displays the following shape: A close-to-ballistic peak around $\Delta\mathbf{u} = \mathbf{0}$ on top of a wide pedestal generated by forward multiple scattering. This statement is confirmed by investigating the angular distributions, $P_{\mathcal{A}}(\Delta\mathbf{u}, z)$ (Supplementary Fig. 13c) and $P_{\mathcal{S}}(\Delta\mathbf{u}, z)$ (Supplementary Fig. 13d), associated with the aberration and scattering matrices, $\boldsymbol{\mathcal{A}}_{\text{out}}$ and $\boldsymbol{\mathcal{S}}_{\text{out}}$, respectively. As anticipated, the aberration component of the $\boldsymbol{\mathcal{T}}-$matrix is associated with a close-to-ballistic peak around $\Delta\mathbf{u} = \mathbf{0}$ (Supplementary Fig. 13c), while its scattering component gives rise to wide distribution of deviation angles in the focal plane (Supplementary Fig. 13d). As illustrated by Supplementary Fig. 13h, a wider angular distribution is observed for $P_{\mathcal{S}}$ at 200 μm than at 50 μm. The angular width of the photon distribution at -10 dB goes from 4deg at $z = 50\mu$m to 10deg at $z = 200\mu$m. This angular dispersion of the transmitted wave-field between the cornea surface and the focal plane is a manifestation of scattering events taking place between those two planes. It thus confirms that our $\boldsymbol{\mathcal{T}}-$matrix estimator indeed contains a forward multiple scattering contribution.

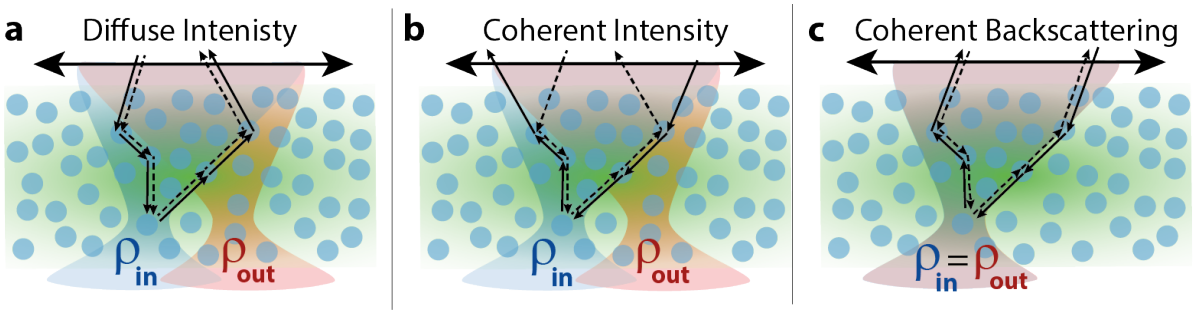


SUPPLEMENTARY FIGURE 13. **Plane wave decomposition of the $\mathcal{T}-$matrix.**. **a.** Definition of the incident and transmitted wave vectors, $\mathbf{k}_{\text{in}}$ and $\mathbf{k}_{\text{out}}$, and their associated angles, θ_{in} and θ_{out}, at the cornea surface and the focal plane. **b-d.** Wave vector deviation distribution of the transmitted wave-field $P_{\mathcal{T}}(\Delta\mathbf{u}, z)$ (**b**), of its aberrated component $P_{\mathcal{A}}(\Delta\mathbf{u}, z)$ (**c**), and of its scattered component $P_{\mathcal{S}}(\Delta\mathbf{u}, z)$ (**d**) [Top: $z = 50\ \mu$m; Bottom: $z = 200\ \mu$m]. **e.** Angular distribution $P_{\mathcal{S}}(\Delta\theta, z)$ of the scattered wave-field at depths z= 50 μm (blue line) and z= 200 μm (red line).

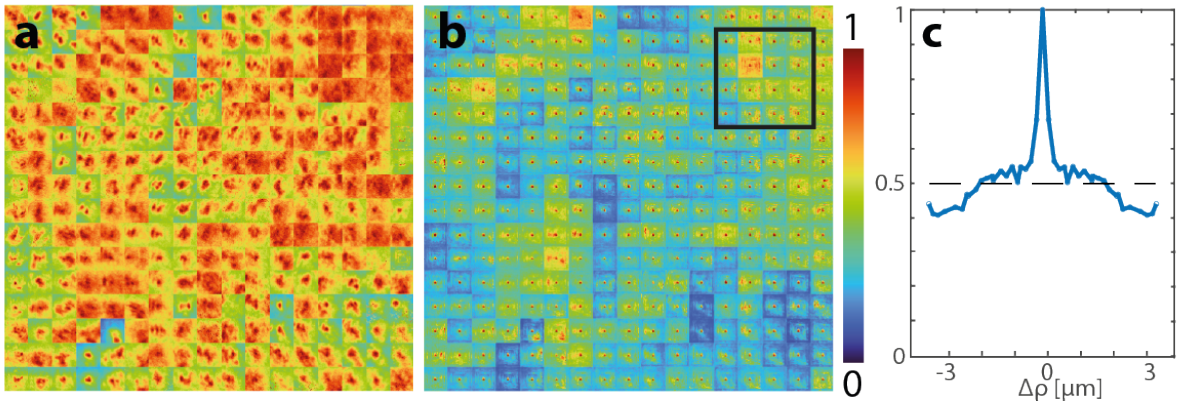
D. Coherent backscattering as a manifestation of multiple scattering

Another key observable to prove the existence of multiple scattering paths is the coherent back-scattering phenomenon. This phenomenon results from the constructive interference between reciprocal multiple scattering paths. Investigated originally in a plane wave basis (**k**-space) [17–19], it manifests as an enhancement by a factor two of the time-gated intensity in the back-scattering direction [20]. Studied in the focused basis (position space), it gives rise to an enhancement by a factor two of the mean intensity at $\Delta\boldsymbol{\rho} = \mathbf{0}$ [14, 21, 22] (Supplementary Fig. 14). This phenomenon is investigated in Supplementary Fig. 15. The initial maps of RPSFs provided by Fig. 4b and reproduced in Supplementary Fig. 15a does not exhibit a clear signature of the CBS because of the aberrations induced by our imaging system that alters its shape [23].

After compensation of the reference arm aberration (Supplementary Fig. 11b) at the



SUPPLEMENTARY FIGURE 14. **Coherent back-scattering phenomenon in the focused basis**. The RPSF is made of two contributions in the multiple scattering regime: **a** A diffuse component which results from the self-interference of each scattering path with itself; **b** A coherent intensity resulting from the interference between reciprocal multiple scattering paths inside the medium. Those paths undergo the same scattering sequence but in reverse order. **c** When the input and output focused beams coincide ($\boldsymbol{\rho}_{\text{in}} = \boldsymbol{\rho}_{\text{out}}$), the interference is constructive and leads to an enhancement by a factor two of the RPSF with respect to the diffuse background. This is the so-called coherent backscattering peak highlighted by Supplementary Fig. 15c.



SUPPLEMENTARY FIGURE 15. **Reflection point spread function in the focused basis.**. **a.** Maps of initial RPSFs at $z = 200$ μm. **b.** Maps of RPSFs at the same depth after compensation of the isoplanatic aberration phase law (Supplementary Fig. 11b) mainly induced by the reference arm. **c.** Radial average of the RPSF averaged over the area surrounded by a black square in panel **b.**.

first step of our aberration correction process, a new map of RPSFs is obtained and shown in Fig. 15b. It exhibits a following shape: A confocal peak due to the single scattering contribution and to the coherent back-scattering phenomenon that results from the construtive

interference between reciprocal multiple scattering paths inside the medium (Supplementary Fig. 14c); on top of a diffusve background resulting from the incoherent summation of each multiple scattering path intensity (Supplementary Fig. 14a).

In absence of noise, the confocal intensity is therefore equal to $I_C = I_S + 2I_M$, with I_S the single scattering intensity and I_M the multiple scattering intensity. The incoherent background directly provides the multiple scattering intensity. The ratio $\beta_C = I_C/I_M$ between the confocal peak and the incoherent background can actually provide an estimate for the multiple scattering rate [14]:

$$\beta_M = I_M/(I_S + I_M) = 1/(\beta_C - 1) \tag{65}$$

or, equivalently, of the single scattering rate

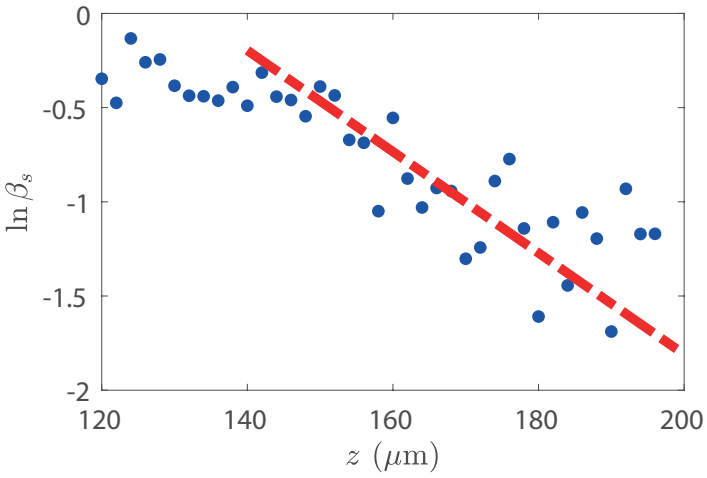
$$\beta_S = I_S/(I_S + I_M) = (\beta_C - 2)/(\beta_C - 1) \tag{66}$$

Note that, in practice, a quantitative measurement of the single/multiple scattering rates is not so easy to perform since the multiple scattering background does not exhibit a flat profile especially at shallow depth [24].

Anyway, a value of β_C close to 2 means a predominant multiple scattering contribution. This is actually what we observe in many parts of the field-of-view, in particular in the area surrounded by a black rectangle in Supplementary Fig. 15b. The radial distribution of the RPSF displayed in Supplementary Fig. 15c shows a CBS enhancement of two, proof that multiple scattering is predominant in this region. At the end of the multi-scale aberration correction process, the maps of RPSF shows a much larger confocal ratio β_C, proof that multiple scattering trajectories have been (at least partially) compensated by our $\boldsymbol{\mathcal{T}}-$matrix estimator.

E. Measuring the Scattering Mean Free Path

In a previous work [25], the scattering mean free path ℓ_s in the cornea was measured by investigating the depth evolution of the confocal intensity. Indeed, in the single scattering regime, under the paraxial approximation and for an homogeneous reflectivity, the time-gated confocal intensity is supposed to decrease as $\exp(-2z/\ell_s)$ if we neglect absorption losses [26, 27].



SUPPLEMENTARY FIGURE 16. Logarithm of the single scattering rate $\ln \beta_S$ versus depth (blue dots) fitted with Eq. 67 (red dashed line).

Unfortunately, here, the cornea is not healthy but oedematous. The depth evolution of the confocal intensity in the stroma is thus strongly impacted by multiple scattering and cannot be used for a measurement of ℓ_s. Moreover, in the epithelium, the different layers of cell make the cornea reflectivity too heterogeneous to provide an exponential decrease of the confocal intensity.

Recently, an alternative strategy has been proposed in presence of multiple scattering [28]. It consists in investigating the depth evolution of the single scattering rate. In 3D, radiative transfer solution indicates the following exponential scaling for β_S [29]:

$$\beta_S(z) \sim \exp\left(-z/\ell_s\right) \tag{67}$$

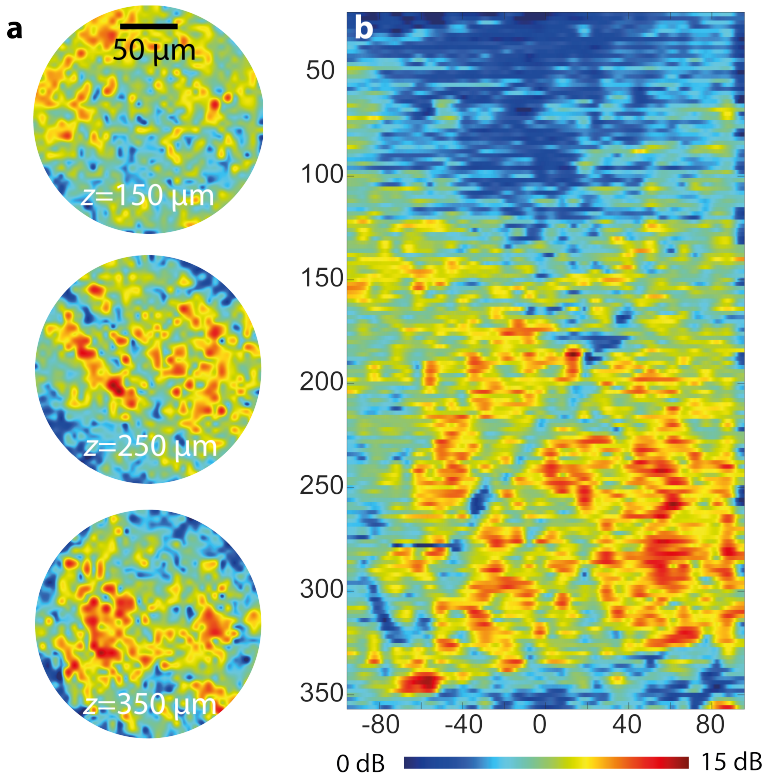
To estimate β_S (Eq. 66), the confocal ratio β_c has been estimated as follows:

$$\hat{\beta}_C(z) = \frac{\max\limits_{\Delta\boldsymbol{\rho}} \{I(\Delta\boldsymbol{\rho}, z)\}}{\min\limits_{\Delta\boldsymbol{\rho}} \{I(\Delta\boldsymbol{\rho}, z)\}} \tag{68}$$

This estimator $\hat{\beta}_C$ relies on the fact that the multiple scattering component of the RPSF exhibits a flat background such that it can estimated with the minimum of $I(\Delta\boldsymbol{\rho}, z)$. This hypothesis is wrong at shallow depth since the diffuse halo grows as $\sqrt{Dt}$, with D the diffusion coefficient. Nevertheless, beyond a few ℓ_s (here 140 μm), the multiple scattering background can be considered as flat as illustrated by Supplementary Fig.15c.

Supplementary Figure 16 displays the depth evolution of the single scattering rate $\beta_S(z)$ computed from $\hat{\beta}_C$ (Eq. 66). It exhibits an exponential decay in the stroma beyond $z = 140$ μm. The single scattering rate cannot be estimated beyond $z = 200$ μm because our estimator of $\beta_C(z)$ starts to be impacted by the experimental noise. Therefore, the fit of $\beta_S(z)$ with Eq. 67 is performed from $z = 140$ to $z = 200$ μm. We find $\ell_s \sim 35$ μm.

F. Quantifying the contrast enhancement



SUPPLEMENTARY FIGURE 17. **Confocal gain provided by the matrix imaging process**. **a-b.** Transverse cross-section of the confocal gain observed for the *en-face* images displayed in Fig. 3b at depths 50 μm, 250 μm and 350 μm within the cornea (scale bar: 50 μm). **c.** Longitudinal cross-section of the confocal gain observed by comparing the B-scan displayed in Fig.3f with its original version shown in Fig. 3c. In each panel, the color scale is in dB.

Supplementary Figure 17 shows the enhancement of the confocal peak before and after RMI. It reaches a maximal value of 30. This gain should scale, in amplitude, as the number P_c of independent coherence grains exhibited by the $\boldsymbol{\mathcal{T}}-$matrix in the pupil plane (see, for

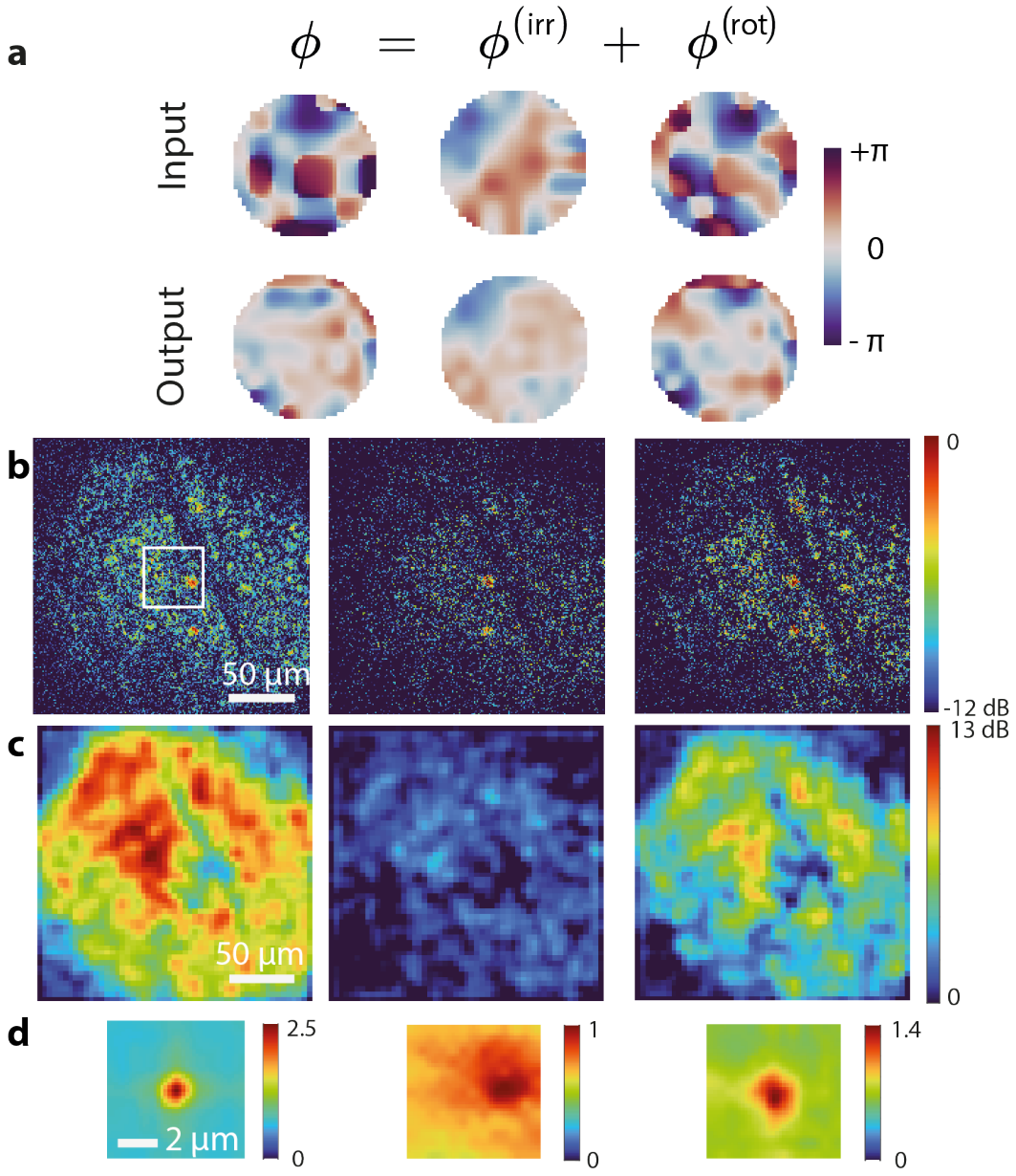
instance, Figs. 4e and f) and that RMI tends to realign in phase by means of a digital optical phase conjugation. Supplementary Figure 17b clearly shows that the confocal gain increases with depth z. Indeed, multiple scattering becomes predominant in depth and the transmission phase laws become more and more complex. Note, however, that given the complexity of phase laws displayed in Figs. 4e and f, we could have expected a larger confocal intensity enhancement. This moderate gain in contrast is explained by the fact that a part of the multiple scattering background is not addressed by RMI.

5. COMPARISON WITH STATE-OF-THE-ART METHODS

A. Comparison between matrix imaging and adaptive optics

The discrimination between aberration and scattering phenomena can be also applied directly to the estimated $\boldsymbol{\mathcal{T}}$-matrix. The interest of such a decomposition is to show the superiority of matrix imaging with respect to conventional AO. Indeed, the latter approach generally relies on Shack Hartmann sensors that only give access to the phase gradient of reflected wave-fronts. Standard numerical integration of this quantity gives access to the irrotational (*i.e* aberrated) component of the wave-front but generally not to the scattering components of the wave-front that exhibits a wealth of optical vortices [16]. On the contrary, the interferometric measurement of the reflected wave-field gives access to this scattering component which is crucial for deep imaging.

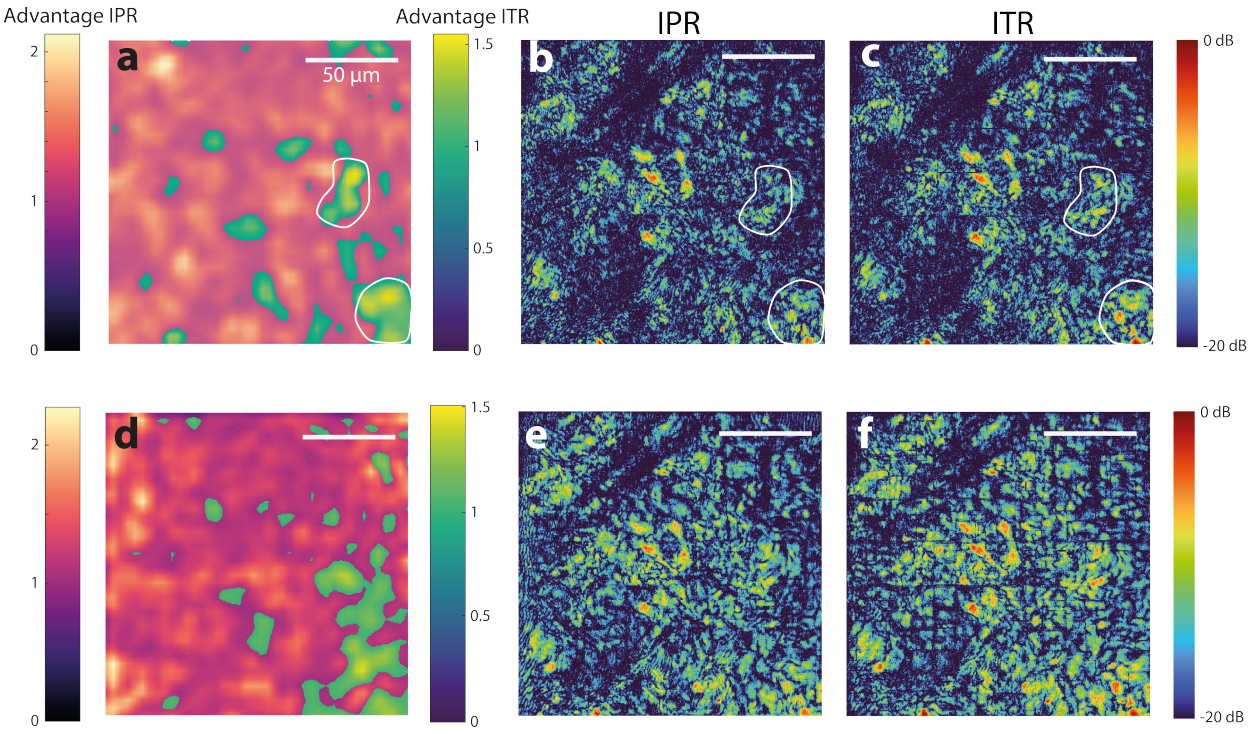
Supplementary Figure 18 illustrates this assertion by first showing the decomposition of the input and output phase laws into their irrotational and curl components (Supplementary Fig. 18a). The access to the latter component is decisive for the compensation of wave distortions since it greatly contributes to the improvement of the confocal image (Supplementary Fig. 18b). This can be quantified by the confocal gain exhibited at the end of the matrix imaging process (Supplementary Fig. 18c) and the corresponding RPSF (Supplementary Fig. 18d). While the access to the curl component of the focusing laws allows us to reach a confocal gain up to 13 dB (right sub-panel of Supplementary Fig. 18c), conventional AO would only allow a compensation of low-order aberrations, giving rise to a weak confocal gain (< 3 dB, middle sub-panel of Supplementary Fig. 18c).



SUPPLEMENTARY FIGURE 18. **Decomposition of the focusing law ϕ extracted by RMI at depth $z = 200$ μm. a.** Examples of input and output phase laws extracted by RMI (left) and their decomposition into irrotational (middle) and curl (right) components. These phase laws correspond to the center of the white rectangle in **b**. **b.** Confocal image obtained using the corresponding focusing laws (scale bar: 50 μm). **c.** Associated confocal gain (scale bar; 50 μm). **d** Example of local RPSF obtained in the white rectangle displayed in panel **b**) (scale bar: 2 μm).

Another advantage of RMI versus AO consists in our ability of simulating any physical experiment in post-processing. If performed experimentally with an adaptive optics set up, the multi-scale compensation of wave distortions described in this paper would require: (*i*) a complex adaptive optics arrangement to compensate for wave distortions both in the sample and reference arms; (*ii*) an extremely long acquisition time since the focusing process would have to be repeated 12 times on each of the 10^8 points of the imaged volume. The performance of matrix imaging is therefore impossible to reach with conventional adaptive optics tools.

B. Comparison between iterative time reversal and iterative phase reversal



SUPPLEMENTARY FIGURE 19. **Multi-scale compensation of wave distortions: Iterative time reversal vs. iterative phase reversal. a.** Ratio between confocal gains obtained at $z = 200$ μm using a ITR or IPR process applied to spatial windows of size $L = 25$ μm (Scale bars: 50 μm). Left colorbar: Ratio between IPR and SVD confocal gains. Right colorbar: Ratio between SVD and IPR confocal gains. **b-c.** Confocal image obtained via IPR (**b**) and ITR (**c**) for $L = 25$ μm. **d-f** Same as in (**a**)-(**c**) but for $L = 6$ μm.

Even though the ITR process does not provide a satisfying estimator at the first iteration of the matrix imaging process (see Supplementary Section 3 A and Supplementary Fig. 2), the multi-scale analysis and continuous balance between input and output correction enable to gradually reduce the size of the virtual scatterer and improves the ITR estimator at depth z =200 μm. In Supplementary Figs. 19b and c, we compare the confocal images provided by ITR and IPR for $L = 25$ μm. Qualitatively, a careful look at the images shows that the ITR correction leads to a smoother image of the sample reflectivity than IPR. This is in agreement with Supplementary Fig. 2 that showed that ITR tends to concentrate on a low spatial frequency spectrum while IPR addresses the whole spatial frequency components of the wave-field. In terms of image resolution, IPR thus shows a better performance than ITR.

To understand why, let us first express the confocal image as a function of the reflection matrix coefficients expressed in the plane wave basis:

$$I(\Delta\boldsymbol{\rho} = \mathbf{0}, \boldsymbol{\rho}_{\text{out}}, z) = \sum_{\mathbf{u}_{\text{in}}} \sum_{\mathbf{u}_{\text{out}}} R(\mathbf{u}_{\text{out}}, \mathbf{u}_{\text{in}}, z) \exp\left[i\frac{2\pi}{\lambda f}(\mathbf{u}_{\text{in}} + \mathbf{u}_{\text{out}}).\boldsymbol{\rho}_{\text{out}}\right] \tag{69}$$

Under an isoplanatic assumption, the coefficients of the reflection matrix in the plane wave basis can be expressed as follows [9]:

$$R(\mathbf{u}_{\text{in}}, \mathbf{u}_{\text{out}}, z) = \mathcal{T}_{\text{out}}(\mathbf{u}_{\text{out}}, z)\tilde{\gamma}(\mathbf{u}_{\text{in}} + \mathbf{u}_{\text{out}}, z)\mathcal{T}_{\text{in}}(\mathbf{u}_{\text{in}}, z) \tag{70}$$

with $\tilde{\gamma}(\mathbf{u}, z) = \int d\boldsymbol{\rho}\gamma(\boldsymbol{\rho}, z) \exp(-i2\pi\mathbf{u}.\boldsymbol{\rho}/(\lambda f))$, the spatial frequency spectrum of the sample reflectivity at depth z. In absence of aberrations, each antidiagonal ($\mathbf{u}_{\text{in}} + \mathbf{u}_{\text{out}}$ = constant) encodes one spatial frequency of the sample reflectivity: $R(\mathbf{u}_{\text{out}}, \mathbf{u}_{\text{in}}, z) = \tilde{\gamma}(\mathbf{u}_{\text{in}} + \mathbf{u}_{\text{out}}, z)$ in the pupil support. $I(\Delta\boldsymbol{\rho} = \mathbf{0}, \boldsymbol{\rho}_{\text{out}}, z)$ is then a satisfying estimator of $\gamma(\boldsymbol{\rho}, z)$ with a transverse resolution only limited by diffraction. In presence of aberrations, phase fluctuations of $\mathcal{T}_{\text{in/out}}$ implies phase distortions between each spatial frequency component of the object while amplitude variations of $\mathcal{T}_{\text{in/out}}$ implies the attenuation of some spatial frequency components of the object.

The compensation of aberrations consists in applying the phase conjugate of the aberration transmittance estimators, $\hat{\mathcal{T}}_{\text{out}}$ and $\hat{\mathcal{T}}_{\text{in}}$, at input and output of the reflection matrix:

$$R''(\mathbf{u}_{\text{out}}, \mathbf{u}_{\text{in}}, z) = \hat{\mathcal{T}}^*_{\text{out}}(\mathbf{u}_{\text{out}}, z)R(\mathbf{u}_{\text{out}}, \mathbf{u}_{\text{in}}, z)\hat{\mathcal{T}}^*_{\text{in}}(\mathbf{u}_{\text{in}}, z) \tag{71}$$

Assuming ITR provides correct estimators of the aberration transmittance ($\hat{\mathcal{T}}_{\text{in/out}} \equiv \mathcal{T}_{\text{in/out}}$) and injecting Eq. 70 into the last equation leads to the following expression for the reflection

matrix corrected by ITR processing:

$$R''_{ITR}(\mathbf{u}_{\text{out}}, \mathbf{u}_{\text{in}}, z) = |\mathcal{T}_{\text{out}}(\mathbf{u}_{\text{out}}, z)|^2 \tilde{\gamma}(\mathbf{u}_{\text{in}} + \mathbf{u}_{\text{out}}, z) |\mathcal{T}_{\text{in}}(\mathbf{u}_{\text{in}}, z)|^2 \tag{72}$$

Because the amplitude of $\mathcal{T}_{\text{in/out}}$ vanishes for high spatial frequency $|\mathbf{u}_{\text{in/out}}|$ (Supplementary Fig. 2b), ITR tends to filter the high spatial frequency component of the object.

On the contrary, IPR converges towards a normalized version of the transmittances $\boldsymbol{\mathcal{T}}_{\text{in/out}}$, such that: $\hat{\mathcal{T}}_{\text{in/out}} \equiv \exp\left(j\arg\left\{\mathcal{T}_{\text{in/out}}\right\}\right)$. Using this last expression of $\hat{\boldsymbol{\mathcal{T}}}_{\text{in/out}}$ and injecting Eq. 70 into 71 leads to the following expression for the reflection matrix corrected by IPR processing:

$$R''_{IPR}(\mathbf{u}_{\text{out}}, \mathbf{u}_{\text{in}}, z) = |\mathcal{T}_{\text{out}}(\mathbf{u}_{\text{out}}, z)| \tilde{\gamma}(\mathbf{u}_{\text{in}} + \mathbf{u}_{\text{out}}, z) |\mathcal{T}_{\text{in}}(\mathbf{u}_{\text{in}}, z)| \tag{73}$$

IPR leaves the spatial frequency spectrum of the reflection matrix unchanged and does not filter the high spatial frequency components of the reflection matrix. Of course, a better compensation of aberration would consist in an inverse filter where the amplitude decrease of $\mathcal{T}_{\text{in/out}}$ could be compensated on top of phase distortions. Nevertheless, this operation is extremely sensitive to noise and suppose a perfect match between the aberration transmittance $\mathcal{T}_{\text{in/out}}$ and their estimators $\hat{\mathcal{T}}_{\text{in/out}}$. This is wrong especially for the phase of $\mathcal{T}_{\text{in/out}}$ at high spatial frequencies where the amplitude of $\hat{\mathcal{T}}_{\text{in/out}}$ vanishes. Therefore, IPR is an adequate compromise between the matched filter operated by ITR that affect the high spatial frequencies of the object and an inverse filter that is extremely sensitive to noise.

In terms of contrast, the relative performance between IPR and ITR can be assessed by investigating the confocal energy at the end of the whole process. Supplementary Fig. 19a shows the ratio between their confocal gains at depth z =200 μm. The IPR process exhibits a better performance on a major part of the field-of-view. The ITR process is only better when it can hang on a highly reflecting structure. In that case, the maximization of backscattered energy on which the ITR process is based can lead to a better result than a criterion based on coherence as done by IPR. In practice, one could apply both IPR and ITR and keep the best option. Nevertheless, for sake of clarity and image continuity, the IPR process has been considered for all figures shown in the accompanying paper. Indeed, for small spatial windows (L = 6 μm), the ITR process leads to an image with strong vignetting effects (Supplementary Fig. 19f), which is a manifestation of a lack of correlations of the

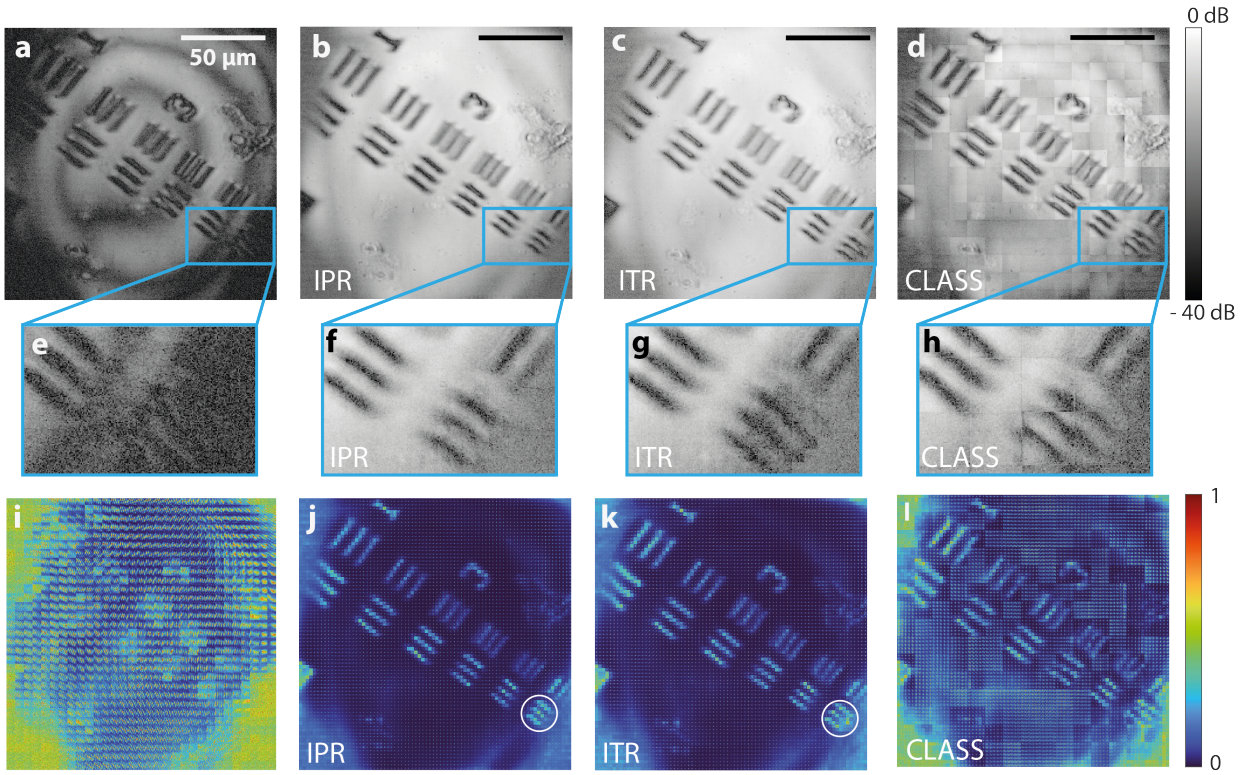
estimator $\hat{\mathbf{T}}$ between adjacent windows. On the contrary, the IPR leads to an estimator whose scattered component $\hat{\mathbf{S}}$ exhibits the expected memory effect for this size of spatial windows (Supplementary Figs. 19e and 7d). Supplementary Figure 19 thus shows the superiority of IPR in terms of spatial resolution for the $\mathbf{T}-$matrix estimation.

The superiority of IPR compared with ITR is also confirmed by the resolution target experiment presented in Supplementary Section 3 H. Supplementary Figure 20 compares the images obtained via IPR and ITR using the multi-scale process described above. The full-field images show a slightly better contrast with IPR (Supplementary Fig. 20b) than ITR (Supplementary Fig. 20c). The zoom on the smallest patterns of the target also shows the benefit of IPR (Supplementary Fig. 20f) compared with ITR (Supplementary Fig. 20g) in terms of resolution. Indeed, the three strips are clearly resolved with IPR, while this pattern remains quite blurred with ITR . This superiority is also confirmed by the corresponding RPSFs displayed in Supplementary Figs. 20j and k. In the area of the smallest pattern surrounded by a white circle, the final RPSFs obtained with IPR display a weaker incoherent background than with ITR. This reference experiment thus confirms the overall superiority of IPR compared with ITR that we have already noticed in the cornea experiment.

C. Comparison between CLASS and RMI

For the last five years, an alternative matrix approach has been developed by W. Choi and colleagues, this is the so-called CLASS algorithm [30–32]. Based on the recording of a time-gated reflection matrix, it exploits its input-output correlations in the plane wave basis to estimate input and output aberration phase laws. The CLASS algorithm amounts to find the aberration phase laws that maximize the confocal intensity in the focused basis. The input and output aberration laws are computed simultaneously and the whole process is then iterated several times to converge towards satisfying phase laws. On the contrary, our algorithm maximizes sequentially the coherence of input and output wave-fields generated by the virtual guide star. It allows us to decrease gradually the size of this guide star and improve the estimation of the $\mathbf{T}$-matrix, while improving its resolution by gradually reducing the size of spatial windows.

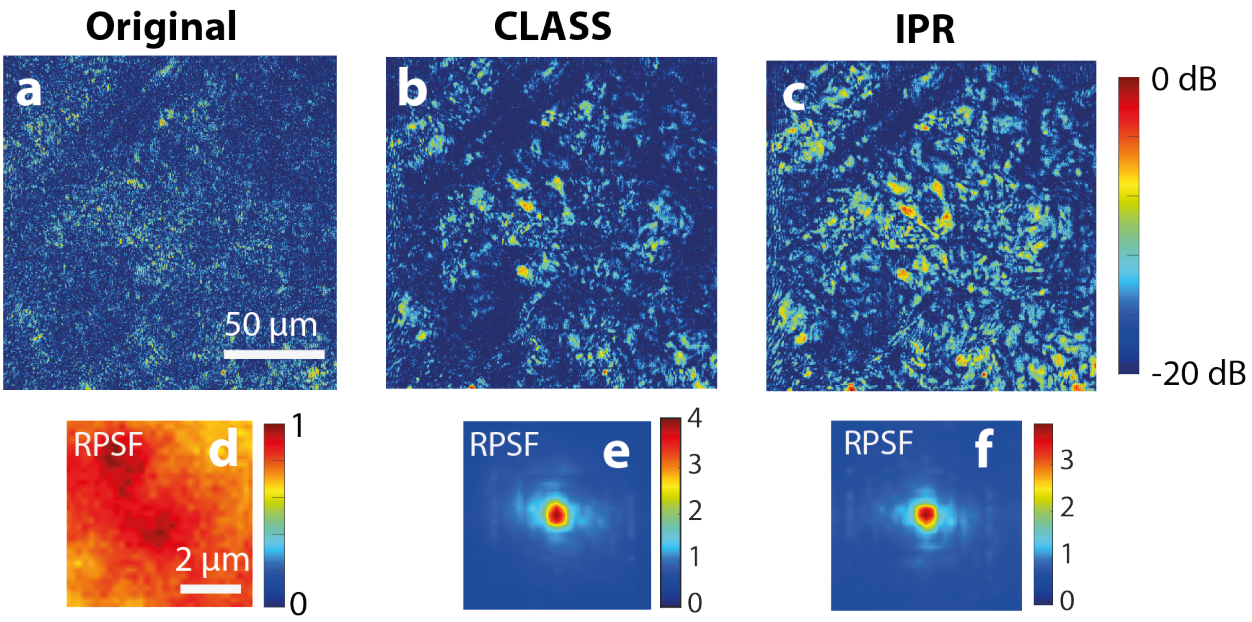
To compare the performance of both approaches, we have applied CLASS on our experimental data at z=200 μm. Supplementary Figure 21 shows the results obtained by



SUPPLEMENTARY FIGURE 20. **Comparison of IPR with other state-of-the-art methods for the resolution target experiment. a-d.** Confocal images (scale bar: 50 μm): Original image (**a**), corrected image using the IPR multi-scale process (**b**), corrected image using the ITR multi-scale process (**c**) and corrected image using the local CLASS algorithm (**d**). **e-h.** Corresponding blowups of the area contained inside the blue rectangle displayed in panels a-d. **i-l.** Corresponding maps of RPSFs (computed over spatial windows of size $L = 2$ μm).

CLASS and IPR when the extension L of spatial windows W_L is sufficiently large to allow the convergence of each method ($L = 14$ μm). Although the corrected RPSF display similar properties in average for each method [Supplementary Figs. 21e and f], the obtained images show significant differences [Supplementary Figs. 21b and c]. On the one hand, the CLASS image seems more contrasted because it tends to focus on the main scatterers of the field-of-view. On the other hand, the IPR image displays a more homogeneous reflectivity across the field-of-view. This difference can be understood by the maximization of the confocal energy operated by CLASS which gives more weight to the most echogenic scatterers to the detriment of weaker reflectivity regions.

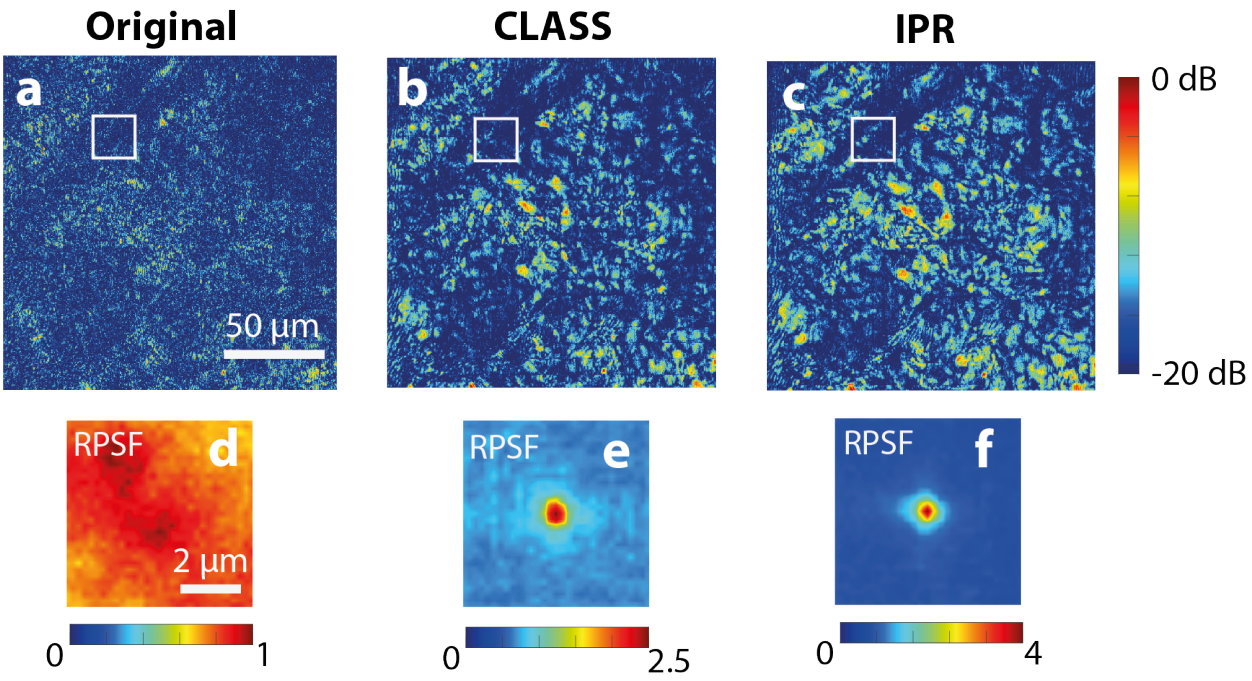
Another difference between CLASS and IPR approach lies in the higher resolution



SUPPLEMENTARY FIGURE 21. **Comparison between CLASS and RMI upon convergence**. **a.** Original confocal image at z=200 μm (scale bar: 50 μm).**b-c.** Corresponding CLASS (**b**) and IPR (**c**) images obtained for spatial windows of size $L = 13$ μm. **d-f.** Means RPSFs corresponding to images displayed in panels (**a**)-(**c**), respectively (scale bar: 2 μm).

capability of the latter method. This assertion is supported by Supplementary Fig. 22 that compares the results of CLASS and IPR for a smaller spatial window ($L = 5.75$ μm). A local RPSF obtained via CLASS is displayed in Supplementary Fig. 22e. It shows an important background, a manifestation of an imperfect compensation of forward multiple scattering. On the contrary, the RPSF obtained at the same location via IPR is close to be ideal (Supplementary Fig. 22d). When looking into details to the CLASS image (Supplementary Fig. 22b), strong vignetting effects can be observed while the IPR image exhibits a continuous reflectivity (Supplementary Fig. 22c).

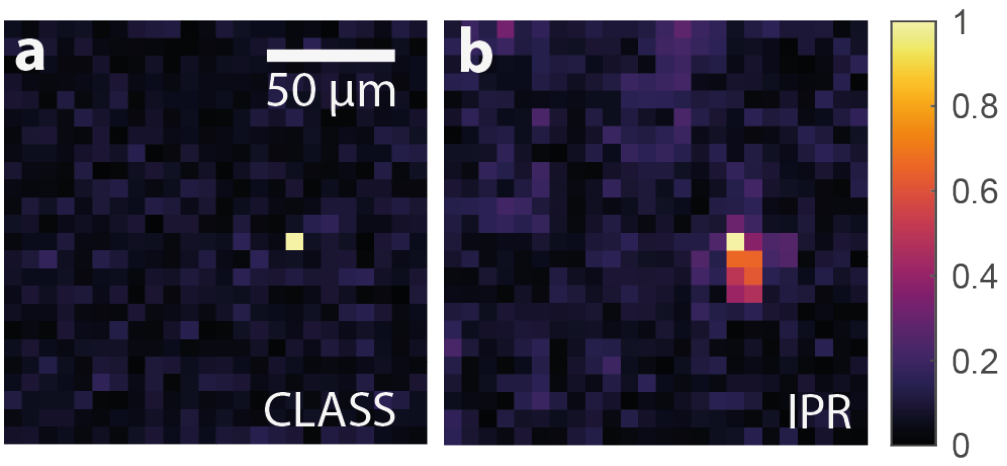
This result can be understood by comparing the spatial correlation properties of the scattering component $\boldsymbol{\mathcal{S}}$ of the $\boldsymbol{\mathcal{T}}-$matrix obtained by CLASS and IPR (see Methods of the accompanying paper). Supplementary Figure 23 shows this correlation map for the mid-point $\mathbf{r}_\mathrm{p}$ of the area displayed with a white square in Supplementary Fig. 22. While the $\boldsymbol{\mathcal{S}}$-matrix derived by IPR preserves a short-range correlation between neighbouring windows (see Supplementary Fig. 23c), the CLASS algorithm leads to a fully spatially incoherent estimator $\hat{\boldsymbol{\mathcal{S}}}$ (see Supplementary Fig. 23a). This observable clearly shows that the IPR



SUPPLEMENTARY FIGURE 22. **Comparison between CLASS and RMI for small isoplanatic patches**. **a.** Original confocal image at z=200 μm (scale bar: 50 μm).**b-c.** Corresponding CLASS (**b**) and IPR (**c**) images obtained for spatial windows of size $L = 6$ μm. **d-f.** Means RPSFs corresponding to images displayed in panels (**a**)-(**c**), respectively (scale bar: 2 μm).

estimator leads to a coherent (i.e physical) compensation of multiple scattering while CLASS leads to an incoherent correction (i.e bucket-like). The result of Supplementary Fig. 23 accounts for the vignetting effects observed for the CLASS image in Supplementary Fig. 22b.

This vignetting effect is also highlighted by the resolution target experiment in Supplementary Fig. 20. The corresponding images obtained with the multi-scale IPR process and the local CLASS algorithm are displayed in Supplementary Figs. 20b and d, respectively. For each method, the size of spatial windows over which aberration phase laws are estimated is $L = 10$ μm. As in the cornea experiment (Supplementary Fig. 23), the CLASS image lacks of continuity between adjacent spatial windows (Supplementary Fig. 20d). The map of RPSFs also shows the imperfect convergence of the CLASS process (Supplementary Fig. 20l). Unlike the RPSFs obtained at the end of the IPR process (Supplementary Figs. 20j), the CLASS RPSFs are far from displaying a diffraction-limited feature. They also show a strong variability across the field-of-view, which is another manifestation of the vignetting effect



SUPPLEMENTARY FIGURE 23. **Memory effect exhibited the forward multiple scattering estimator: Comparison between CLASS and RMI**. Spatial correlation function $C_S(\mathbf{r}_\mathrm{p}, \mathbf{r}'_\mathrm{p})$ of the scattering component $\hat{\mathbf{S}}$ for a given point $\mathbf{r}'_\mathrm{p}$. **a.** CLASS. **b.** RMI. The depth is $z = 200$ μm and the size of spatial windows is $L = 6$ μm. Scale bar: 50 μm.

observed in the full-field CLASS image (Supplementary Figs. 20d). The resolution target experiment thus confirms the superiority of a multi-scale IPR process with respect to the local CLASS algorithm.

6. GLOSSARY

operator	definition
$\mathbf{R} = [R(\boldsymbol{\rho}_{\text{in}}, \boldsymbol{\rho}_{\text{out}}, z)]$	reflection matrix in the focused basis
$\mathbf{R}_{\text{in/out}} = [R_{\text{in}}(\Delta\boldsymbol{\rho}_{\text{in/out}}, \boldsymbol{\rho}_{\text{out/in}}, z)]$	de-scanned matrix at input/output
$\mathbf{D}_{\text{in/out}} = [D(\mathbf{u}_{\text{in/out}}, \boldsymbol{\rho}_{\text{out/in}}), z]$	input/output distortion matrix
$\mathbf{H}_{\text{in/out}} = [H_{\text{in}}(\boldsymbol{\rho}_{\boldsymbol{s}}, \boldsymbol{\rho}_{\text{in/out}}, z)]$	input/output focusing matrix
$\mathbf{T}_0 = [T_0(\mathbf{u}, \boldsymbol{\rho})]$	Fourier transform operator
$\mathbf{C}_{\text{in/out}} = [C_{\text{in/out}}(\mathbf{u}_{\text{in/out}}, \mathbf{u}'_{\text{in/out}}, \mathbf{r}_p)]$	input/output pupil correlation matrix of $\mathbf{D_{in}}$
$\mathbf{C}_H = [C_H(\mathbf{u}, \mathbf{u'})]$	correlation matrix associated with a virtual reflector of reflectivity $\lvert H(\boldsymbol{\rho_s})\rvert^2$
$\mathbf{T}_{\text{in/out}} = [T_{\text{in/out}}(\mathbf{u}_{\text{in/out}}, \mathbf{r}_p)]$	input/output transmission matrix
$\boldsymbol{\mathcal{T}}_{\text{in/out}} = [\mathcal{T}_{\text{in/out}}(\mathbf{u}_{\text{in/out}}, \mathbf{r}_p)]$	input/output transmittance matrix
$\hat{\boldsymbol{\mathcal{T}}}_{\text{in/out}} = [\mathcal{T}_{\text{in/out}}(\mathbf{u}_{\text{in/out}}, \mathbf{r}_p)]$	estimator of the input/output transmittance matrix
$\boldsymbol{\phi}_{\text{in/out}} = [\phi_{\text{in/out}}(\mathbf{u}_{\text{in/out}}, \mathbf{r}_p)]$	phase of the input/output transmission matrix estimator
$\boldsymbol{\mathcal{A}}_{\text{in/out}} = [\mathcal{A}_{\text{in/out}}(\mathbf{u}_{\text{in/out}}, \mathbf{r}_p)]$	input/output aberration matrix
$\boldsymbol{\mathcal{S}}_{\text{in/out}} = [\mathcal{S}_{\text{in/out}}(\mathbf{u}_{\text{in/out}}, \mathbf{r}_p)]$	input/output forward multiple scattering matrix

SUPPLEMENTARY TABLE 1. **Glossary of the operators used in this study**

SUPPLEMENTARY REFERENCES

[1] J. Mertz, *Introduction to Optical Microscopy*, second edition ed. (Cambridge University Press, Cambridge, United Kingdom ; New York, NY, 2019).

[2] A. F. Fercher, Optical coherence tomography., J. Biomed. Opt. **1**, 157 (1996).

[3] A. Badon, G. Lerosey, A. C. Boccara, M. Fink, and A. Aubry, Retrieving Time-Dependent Green's Functions in Optics with Low-Coherence Interferometry, Phys. Rev. Lett. **114**, 023901 (2015).

[4] A. Badon, D. Li, G. Lerosey, A. Claude Boccara, M. Fink, and A. Aubry, Spatio-temporal imaging of light transport in highly scattering media under white light illumination, Optica **3**, 1160 (2016).

[5] V. Barolle, J. Scholler, P. Mecê, J.-M. Chassot, K. Groux, M. Fink, A. C. Boccara, and A. Aubry, Manifestation of aberrations in full-field optical coherence tomography, Opt. Express **29**, 22044 (2021).

[6] A. Badon, V. Barolle, K. Irsch, A. C. Boccara, M. Fink, and A. Aubry, Distortion matrix concept for deep optical imaging in scattering media, Sci. Adv. **6**, eaay7170 (2020).

[7] J.-L. Robert and M. Fink, Green's function estimation in speckle using the decomposition of the time reversal operator: Application to aberration correction in medical imaging, J. Acoust. Soc. Am. **123**, 866 (2008).

[8] W. Lambert, L. A. Cobus, J. Robin, M. Fink, and A. Aubry, Ultrasound matrix imaging – Part II: The distortion matrix for aberration correction over multiple isoplanatic patches, IEEE Trans. Med. Imag. **41**, 3921 (2022).

[9] W. Lambert, L. A. Cobus, T. Frappart, M. Fink, and A. Aubry, Distortion matrix approach for ultrasound imaging of random scattering media, Proc. Natl. Acad. Sci. U. S. A. **117**, 14645 (2020).

[10] C. Prada and M. Fink, Eigenmodes of the time reversal operator: A solution to selective focusing in multiple-target media, Wave Motion **20**, 151 (1994).

[11] C. Prada, S. Manneville, D. Spoliansky, and M. Fink, Decomposition of the time reversal operator: Detection and selective focusing on two scatterers, J. Acoust. Soc. Am. **99**, 2067 (1996), publisher: Acoustical Society of America.

[12] R. Mallart and M. Fink, Adaptive focusing in scattering media through sound-speed inhomogeneities: The van Cittert Zernike approach and focusing criterion, J. Acoust. Soc. Am. **96**,

3721 (1994).

[13] S. Silverstein, Ultrasound scattering model: 2-d cross-correlation and focusing criteria-theory, simulations, and experiments, IEEE Trans. Ultrason. Ferroelectr. Freq. Control **48**, 1023 (2001).

[14] W. Lambert, L. A. Cobus, M. Couade, M. Fink, and A. Aubry, Reflection Matrix Approach for Quantitative Imaging of Scattering Media, Phys. Rev. X **10**, 021048 (2020).

[15] T. Wu, P. Berto, and M. Guillon, Appl. Phys. Lett. **118**, 251102 (2021).

[16] T. Wu, Y. Zhang, B. Blochet, P. Arjmand, P. Berto, and M. Guillon, Single-shot digital optical fluorescence phase conjugation through forward multiple-scattering samples, Sci. Adv. **10**, adi1120 (2023).

[17] M. P. V. Albada and A. Lagendijk, Observation of weak localization of light in a random medium, Phys. Rev. Lett. **55**, 2692 (1985).

[18] P.-E. Wolf and G. Maret, Weak localization and coherent backscattering of photons in disordered media, Phys. Rev. Lett. **55**, 2696 (1985).

[19] E. Akkermans, P. E. Wolf, R. Maynard, and G. Maret, Theoretical study of the coherent backscattering of light by disordered media, J. Phys. France **49** (1988).

[20] A. Tourin, A. Derode, P. Roux, B. A. van Tiggelen, and M. Fink, Time-dependent coherent backscattering of acoustic waves, Phys. Rev. Lett. **79**, 3637 (1997).

[21] E. Larose, L. Margerin, B. A. van Tiggelen, and M. Campillo, Weak localization of seismic waves, Phys. Rev. Lett. **93**, 048501 (2004).

[22] A. Aubry and A. Derode, Ultrasonic imaging of highly scattering media from local measurements of the diffusion constant: Separation of coherent and incoherent intensities, Phys. Rev. E **75**, 026602 (2007).

[23] L. A. Cobus, G. Maret, and A. Aubry, Crossover from renormalized to conventional diffusion near the 3D anderson localization transition for light, Phys. Rev. B **106**, 014208 (2022), https://arxiv.org/abs/2109.11188.

[24] W. Lambert, J. Robin, L. A. Cobus, M. Fink, and A. Aubry, Ultrasound matrix imaging – Part I: The focused reflection matrix, the F-factor and the role of multiple scattering, IEEE Trans. Med. Imag. **41**, 3907 (2022).

[25] R. Bocheux, P. Pernot, V. Borderie, K. Plamann, and K. Irsch, Quantitative measures of corneal transparency, derived from objective analysis of depth-resolved corneal images, demonstrated

with full-field optical coherence tomographic microscopy, PLOS ONE **14**, e0221707 (2019).

[26] A. Badon, A. C. Boccara, G. Lerosey, M. Fink, and A. Aubry, Multiple scattering limit in optical microscopy, Opt. Express **25**, 28914 (2017).

[27] U. Tricoli and R. Carminati, Modeling of full-field optical coherence tomography in scattering media, J. Opt. Soc. Am. A **36**, C122 (2019).

[28] C. Brütt, A. Aubry, B. Gérardin, A. Derode, and C. Prada, Weight of single and recurrent scattering in the reflection matrix of complex media, Phys. Rev. E **106**, 025001 (2022).

[29] A. Goicoechea, C. Brutt, F. Bureau, A. Le Ber, C. Prada, and A. Aubry, Reflection measurement of the scattering mean free path at the onset of multiple scattering, arXiv:2401.02246 10.48550/arXiv.2401.02246 (2024).

[30] S. Kang, P. Kang, S. Jeong, Y. Kwon, T. D. Yang, J. H. Hong, M. Kim, K. Song, J. H. Park, J. H. Lee, M. J. Kim, K. H. Kim, and W. Choi, High-resolution adaptive optical imaging within thick scattering media using closed-loop accumulation of single scattering, Nat. Commun. **8**, 2157 (2017).

[31] S. Yoon, H. Lee, J. H. Hong, Y.-S. Lim, and W. Choi, Laser scanning reflection-matrix microscopy for aberration-free imaging through intact mouse skull, Nat. Commun. **11**, 5721 (2020).

[32] Y. Kwon, J. H. Hong, S. Kang, H. Lee, Y. Jo, K. H. Kim, S. Yoon, and W. Choi, Computational conjugate adaptive optics microscopy for longitudinal through-skull imaging of cortical myelin, Nat. Commun. **14**, 105 (2023).